Efficiency of magnesium hydroxide as engineering seal in the geological sequestration of CO_2

Gabriela Dávila [a,b,c,*], Jordi Cama[a,b,], Salvador Galí[d], Linda Luquot[a,b,] and Josep M. Soler [a,b,]

[a] Institute of Environmental Assessment and Water Research (IDAEA), CSIC.

Jordi Girona 18-26, 08034 Barcelona, Catalonia, Spain.

[b] Associated Unit: Hydrogeology Group (UPC-CSIC).

[c] Department of Civil and Environmental Engineering, Universitat Politècnica de Catalunya (UPC).

Jordi Girona 1-3, 08034 Barcelona, Catalonia, Spain.

[d] Department of Crystallography, Mineralogy and Mineral Deposits, Faculty of Geology, University of Barcelona.

Martí i Franquès s/n, 08028 Barcelona, Catalonia, Spain.

*Corresponding author: Gabriela Dávila (gabgeo@cid.csic.es)
Jordi Girona 18-26, Barcelona 08034. Catalonia, Spain
Tel #:+34 934006100
Fax #: +34932045904

Abstract

Injection of CO_2 at depth will cause the acidification of groundwater. As a preliminary study for the potential use of MgO as an alternative to Portland cement in injection wells, MgO carbonation has been studied by means of stirred batch experiments under subcritic (pCO_2 of 10 and 50 bar and T of 25, 70 and 90 °C) and supercritic (pCO_2 of 74 bar and T of 70 and 90 °C) CO_2 conditions.

Magnesium oxide reacts with CO_2-containing and Ca-rich water nearly equilibrated with respect to calcite. MgO quickly hydrates to brucite ($Mg(OH)_2$) which dissolves causing the precipitation of magnesium carbonate phases. Precipitation of these secondary phases (magnesite and/or metastable phases such as nesquehonite ($MgCO_3 \cdot 3H_2O$) or hydromagnesite ($Mg_5(CO_3)_4(OH)_2 \cdot 4(H_2O)$) depends on pCO_2, temperature and solid/water content. In a constant solid/water ratio, the precipitation of the non-hydrated Mg carbonate is favored by increasing temperature and pCO_2.

The experimental variation of Mg and Ca concentrations and pH over time at the different temperatures and pCO_2 has been simulated using the CrunchFlow reactive transport code. Simulations reproduce the experimental evolution of the aqueous concentrations and indicate a decrease in porosity when increasing temperature and pCO_2. This decrease in porosity would be beneficial for the sealing properties of the cement. These results have been used in the simulation of an application case with a deep borehole surrounded by MgO cement at 90 °C.

Keywords: CO_2 sequestration, MgO-based cement, porosity, Mg-Carbonates, brucite dissolution, precipitation.

1. Introduction

CO_2 storage in large volumes such as in saline geological formation is proposed as one of the alternatives for reduction of CO_2 emissions in the atmosphere. The CO_2 phase is injected into the deep reservoir formations through wells. After drilling, the wells were cemented in the hole with a steel pipe (casing). It is a common practice to inject cement into the space between the well casing and the rock (Rahman et al., 1988). The cement acts as a barrier to isolate the reservoir from the environment and to prevent CO_2 leakage and pollution either from or to the reservoir (Nogues et al., 2011). Nevertheless, the cement becomes a potential pathway to CO_2 leakage. The leakage may occur through the interface between casing and cement, cement plug and casing, or through the cement pore space and fractures (Gasda et al., 2004; Celia et al., 2005; Watson and Bachu, 2008; Jung et al., 2014).

Portland cement (PC), used predominantly as concrete in conventional wells, will react with the CO_2 when water is present dissolving the major phases of the hydrated cement (portlandite and C-S-H gel) and forming calcium carbonate (calcite, aragonite, vaterite; Kutchko et al., 2007). Carbonation may be associated with significant changes in the flow, transport and mechanical properties of the cement and could lead to a loss of insulating properties (Dewaele et al., 1991; Scherer et al., 2005; Bachu and Bennion 2009; Kutchko et al., 2008; Duguid, 2009; Luquot et al., 2013). Laboratory studies suggest that Ca-based cement paste samples with a low water-to-cement (w/c) ratio may not be as susceptible to CO_2 attack due to the formation of a quasi-impermeable carbonate layer at the contact between the CO_2-rich brine and the cement, which forms a barrier to further cement degradation (Kutchko et al., 2007; 2008; Jacquemet et al.,

2012). These laboratory findings are supported by the strong performance of PC in boreholes that have been exposed to CO_2 for 30 years (Carey et al., 2007).

Nonetheless, as explained below, other laboratory studies showed differences in carbonation processes, which affected the flow, transport and mechanical properties. The cement composition varied according to the American Petroleum Institute (API) specification of the oil and gas industry, depending on temperature and pressure (from class A to G cements). Under atmospheric pressure (P) and between 20-50 °C conditions, in a core with cement pastes embedded in sandstones and limestones, it was observed that the resulting permeability depended on the interface rock in which the faster degradation occurred (Duguid et al., 2011). By contrast, at the same P and ambient temperature (T = 25 °C) with the flow of CO_2-rich brine through cement cores for 4 and 8 weeks, the formation of three distinct regions was observed: at the solid/fluid contact most of the portlandite was lost, leading to an increase in Ca concentration and promoting Ca carbonation, followed by a moderate porous layer and ending with an unaltered cement (Yalcinkaya et al., 2011). Under high pressure and between 60 to 90 °C conditions, the PC was highly reactive and dissolved Mg common in deep saline brines would react with the wellbore cement to form poorly-crystalline solids (Carroll et al., 2011). The decrease in porosity (ϕ) and permeability (k) increases the ability of the material to fill (healing) pre-existing fractures, improving the sealing properties of the cement over time (Liteanu and Spiers, 2011). At least constant k was obtained by C-S-H dissolution and k decrease was only observed when a Si-rich amorphous phase precipitated (Abdoulghafour et al., 2013). When the flow rate is insufficient to remove the results of carbonation reactions, they probably formed a protective layer, thus preventing permeability enhancement (Bachu and Bennion, 2009).

Given the time scale associated with geological CO_2 sequestration, the use of alternative cements that are not subject to the harmful effects of carbonation would be advisable. Reactive magnesium oxide (MgO) can be successfully blended together with Portland cement and result in improvements in sustainability, strength and many other properties of concretes (Harrison, 2001). The advantages of MgO over Portland cement include precipitation of higher resistance secondary phases, less sensitivity to impurities, and that it can be obtained as a by-product from other industrial processes (Unluer and Tabbaa, 2013). Mo et al. (2014) showed that expansion properties of MgO, used as an

expansive additive, depend on its hydration reactivity and microstructure which are influenced by the calcination conditions.

In this paper, caustic magnesia (MgO) is studied as an alternative to Portland cement, not only to be used in the space between the well casing and the rock but also to seal rock fractures (grouting). At this stage, the reactivity of MgO, excluding MgO-Portland cement blends, is studied in a range of pCO_2 and T relevant for CO_2 injection cases. Also, MgO carbonation is the subject of this study without accounting for the mechanical and physical properties of the material (e.g. MgO slurry density, hardening/curing time of the slurries, mechanical stability seals, etc.). Certainly, the impact of the change in these properties in the MgO-base cement should be pondered in the event of the material being of industrial use. The overall MgO-carbonation process is said to occur when MgO hydrates rapidly to form brucite ($Mg(OH)_2$) (see reactions below). When brucite dissolves in a Ca-rich and CO_2-saturated solution, the solution supersaturates with respect to Ca and/or Mg carbonates (e.g., dolomite ($CaMg(CO_3)_2$), nesquehonite ($MgCO_3{\cdot}3(H_2O)$), hydromagnesite ($Mg_5(CO_3)_4(OH)_2{\cdot}4(H_2O)$) and magnesite ($MgCO_3$)). Different conditions of pCO_2, T, and solid/water ratio determine the formation of these carbonates. In turn, MgO secondary phases could hydrate at different rates. The overall process is summarized with the following reactions:

$$MgO + H_2O \rightarrow Mg(OH)_2 \quad (1)$$

$$Mg(OH)_2 + 2H^+ \rightarrow Mg^{+2} + 2H_2O \quad (2)$$

$$Mg^{2+} + Ca^{2+} + 2CO_3^{2-} \rightarrow 2(Ca,Mg)CO_3 \quad (3)$$

$$Mg^{2+} + CO_3^{2-} + nH_2O \rightarrow MgCO_3 \cdot nH_2O \quad (4)$$

The molar volumes of the implicated minerals ($cm^3\ mol^{-1}$) [($Mg(OH)_2$ (24.63), $CaCO_3$ (36.93), $MgCO_3$ (28.02), $CaMg(CO_3)_2$ (64.37), $Mg_5(CO_3)_4(OH)_2{\cdot}4(H_2O)$ (208.08), $MgCO_3{\cdot}3(H_2O)$ (75.47)], with large molar volumes for the secondary phases, favor a potential decrease in porosity and hence the sealing of cracks in cement structures, preventing CO_2 leakage.

The MgO-CO_2-H_2O system exhibits a complex behavior due to the large number of possible phases and to the strong kinetic inhibitions that are dependent on temperature, partial pressure of CO_2, salinity and possibly other parameters (Sayles and Fyfe, 1973;

O'Connor et al., 2001; Wolf et al., 2004; Hänchen et al., 2008; Unluer and Tabbaa, 2013; Gautier et al., 2014; Kristova et al., 2014). At low pCO_2 (0.015-15 bar), nesquehonite is thermodynamically and chemically stable below 50 °C (Ferrini et al., 2009; Zhao et al., 2010) and precipitation of hydromagnesite requires a temperature greater than 50 °C (Back et al. (2011). Under CO_2 supercritical conditions (pCO_2 = 82 bar), carbonation of brucite into nesquehonite takes place at 50 °C and its conversion into magnesite at 75 °C (Schaef et al., 2011).

Although these works shed light on MgO carbonation, it is considered necessary to study this process under conditions that are representative of those encountered in CO_2 storage. In particular, taking into account that Ca-rich brines are commonly found in saline aquifers such as the one in the Hontomín test site (Spain) (Dávila et al., 2011, 2015), the goal of this work is to study the overall process of MgO carbonation in aqueous solutions equilibrated with respect to calcite under subcritical (pCO_2 of 10 and 50 bars and T of 25, 70 and 90 °C) and supercritical (pCO_2 of 74 bar and T of 70 and 90 °C) CO_2 conditions. Stirred batch experiments were conducted in an autoclave and the experimental results were numerically reproduced using the CrunchFlow reactive transport code (Steefel et al., 2015). Finally, a possible application case (CO_2-rich water interacting with MgO in a borehole), using the laboratory results, was simulated.

2. Materials and methods

2.1 Sample preparation and characterization

The commercial MgO Magna L manufactured by Magnesitas Navarras S.A. was selected and ground to a grain size between 60 and 150 µm. Thereafter, the ground sample was washed three times with pH 1 solution (HCl) to dissolve the CaO fraction and obtain a pure MgO sample. The washed sample was totally dried in the oven at 45 °C and ground up to further characterization. X-ray diffraction (XRD) was performed on thoroughly crushed samples using a Bruker D8 A25 Advance X-ray diffractometer θ-θ, with CuKα1 radiation, Bragg-Brentano geometry, and a position sensitive LynxEyeXE detector. The diffractograms were obtained from 4º to 120º of 2-Theta with a step of 0.015º and a counting time of 0.5s and the sample in rotation. The crystalline phase identification was carried out by using the computer program ''EVA'' (Produced by Bruker). The software TOPAS (Bruker AXS TOPAS, general profile and structure

analysis software for powder diffraction data, V2.0, Bruker AXS, Karlsruhe, Germany, 2000) with the fundamental parameter approach was used for Rietveld refinement. The optimized parameters were background coefficients, zero-shift error, peak shape parameters, scale factor and cell parameters. The values of the pattern dependents, Rwp, disagreement factor, and statistical reliability factor of Bragg, RB, were evaluated and they indicated that the fits were satisfactory. The Rwp obtained in all these measurements were less than 20, which indicates an accurate Rietveld refinement. Mineralogical composition of the washed sample was determined by Rietveld analyses with an uncertainty of 3 *wt.*% (Young, 1995). The sample was mainly made up of MgO (86.9 *wt.*%), with minor amounts of $CaCO_3$ (3.1 *wt.*%), SiO_2 (5.3 *wt.*%), $Mg_5(CO_3)_4(OH)_2{\cdot}4H_2O$ (1.2 *wt.*%), $CaMg(CO_3)_2$ (0.6 *wt.*%), and $Ca(OH)_2$ (3.1 *wt.*%). Table 1 lists the calculated *wt.*% of the minerals fitted with the porosity. Scanning electron microscopy (SEM) was performed on C-coated samples using a Hitachi H-4100FE instrument under a 15-20 kV potential. XRD and SEM were used to examine the solid samples before and after the experiments. The BET specific surface area was measured using 5-point N_2 adsorption isotherms with a Micromeritics ASAP 2000 surface area analyzer. The specific surface area (A_{BET}) of the non-reacted sample was 4.8 ± 0.02 m^2 g^{-1}.

2.2 Input solution

Calcite fragments were poured into 2L of Millipore MQ water (18.2 MΩ cm) at room *T* and atmospheric pCO_2 conditions. The mixture was stirred for approximately 34 d. The resulting solution was filtered using a 0.1 µm nucleopore polycarbonate membrane filter. The measured pH and Ca concentration was 7.77 and 1.86×10^{-4} mol kg_w^{-1}, respectively. The equilibrium calculations using first, the CrunchFlow code (Steefel et al., 2015) and the EQ3/6 database (Wolery et al., 1990), and secondly, the PhreeqC (v.3) code (Parkhurst and Appelo, 2013) and the Llnl and Phreeqc databases, showed that the injected solution was undersaturated with respect to calcite (saturation index *SI* = -1.28 ± 0.03) under atmospheric conditions ($pCO_2 = 390 \times 10^{-6}$ bar and $C_{CO2} = 3.832 \times 10^{-4}$ mol kgw^{-1}).

2.3 Experimental setup and batch experiments

33 stirred batch experiments at different temperature (25, 70 and 90 °C) and pCO_2 (10, 50 and 74 bar) were conducted in an autoclave system (Fig. 1). The experimental time spans varied from 5 to 97 hours. The solid/solution ratio was kept constant in all the experiments (5.3 g MgO/47.7 mL of Ca-rich water). Once solid and solution were placed in the autoclave, the desired pCO_2 and temperature were applied and maintained constant during the whole experimental run. In the experiments run at T > 25 °C, when the desired temperature in the autoclave was reached, the solution and the solid were placed in it and CO_2 was injected. The experiments were stirred at 500 rpm to guarantee homogeneous composition of the bulk solution. At the end of the experiment, liquid samples were taken from a sample collector (Fig. 1). Immediately, 10 mL of the collected solution were syringed, filtered using a 0.2 μm Nucleopore polycarbonate membrane filter and acidified in 2% HCl solution (pH = 1) to avoid precipitation of Mg-bearing carbonate phases during sample depressurization. Total concentrations of Mg and Ca were measured by ICP-AES in a Thermo Jarrel-Ash instrument with CID detector. The detection limits were 10 and 200 mg L^{-1}, respectively, and the analytical error was estimated to be 3%.

3. Description of the reactive transport code

Reactor transport modeling was performed using CrunchFlow (Steefel et al., 2015). The CrunchFlow code solves numerically the mass balance of solutes expressed as

$$\frac{\partial(\phi C_i)}{\partial t} = \nabla \cdot (\mathbf{D}\,\nabla C_i) - \nabla(\mathbf{q} C_i) + R_i \qquad (i = 1, 2, 3, \ldots, n) \quad (5)$$

where ϕ is porosity, C_i is the concentration of component i (mol m^{-3}), **q** is the Darcy velocity ($m^3m^{-2}s^{-1}$), R_i is the total reaction rate affecting component i (mol m^{-3} rock s^{-1}) and **D** is the combined dispersion-diffusion coefficient (m^2s^{-1}).

The total reaction rate R_i is given by

$$R_i = -\sum_m \nu_{im} R_m \qquad (6)$$

where R_m is the rate of precipitation (R_m>0) or dissolution (R_m<0) of mineral m in mol m^{-3} rock s^{-1} , and ν_{im} is the number of the moles of i in mineral m.

The reaction rate laws used in the calculations are of the form (Lasaga, 1998)

$$R_m = -A_m \sum_{terms} k_{m,T} a_{H+}^{n_{H+}} \left(\prod_i a_i^{n_i} \right) f_m(\Delta G_r) \tag{7}$$

where A_m is the mineral surface area in m^2 m^{-3} rock, $k_{m,T}$ is the temperature dependent reaction rate constant in mol m^{-2} s^{-1}, $a_{H+}^{n_{H+}}$ is the term describing the effect of pH on the rate, $a_i^{n_i}$ is the term describing a catalytic/inhibitory effect on the rate by another species, and $f_m(\Delta G_r)$ is the function describing the rate dependence on the solution saturation state. The summation term indicates that several parallel rate laws may be used to describe the dependence of the rate on pH or on other species.

The $f_m(\Delta G_r)$ function is defined as

$$f_m(\Delta G_r) = \left(\mathbf{1} - \left(\frac{IAP}{K_{eq}} \right)^{m_2} \right)^{m_1} \tag{8}$$

The Gibbs free energy of the reaction (ΔG_r; J mol^{-1}) is expressed as

$$\Delta G_r = RT \ln\left(\frac{IAP}{K_{eq}} \right) \tag{9}$$

where *IAP* is the ionic activity product of the solution with respect to the mineral, K_{eq} is the equilibrium constant for that mineral reaction (ionic activity product at equilibrium), m_1 and m_2 exponents allow for nonlinear dependencies on the affinity term and are normally taken from experimental studies, R is the gas constant (J mol^{-1} K^{-1}) and T is absolute temperature (K).

The rate constant at temperature T ($k_{m,T}$) is calculated from

$$k_{m,T} = k_{m,25} \exp\left(\frac{Ea}{R} \left(\frac{1}{T_{25}} - \frac{1}{T} \right) \right) \tag{10}$$

where $k_{m,25}$ is the rate constant at 25 ^{o}C and E_a is the apparent activation energy of the overall reaction (J mol^{-1}). Change in mineral surface area A_m (m^2 mineral m^{-3} rock) is calculated assuming that area is proportional to the volume fraction of the mineral to the power 2/3.

4. Model parameters

4.1 Solid and solution parameters

Assuming that MgO quickly hydrates to brucite (e.g., Fruhwirth et al., 1985), it was considered that brucite was the magnesium phase that dissolved leading to formation of Mg-carbonate minerals. Accordingly, the initial solid was composed of 2.43 *vol.*% brucite, 0.1 *vol.*% calcite, 0.18 *vol.*% quartz, 0.05 *vol.*% hydromagnesite, 0.02 *vol.*% dolomite and 0.12 *vol.*% portlandite with a porosity equal to 97 %. This porosity was calculated from the ratio between the volume of water ($V_{solution}$) and the volume of water plus solid ($V_{solution}$ + V_{solid}) in the experiments. For each experiment (T, pCO$_2$), only the most abundant secondary Mg carbonate phases, that were quantified by XRD-Rietveld analyses, were taken into account (see *Section.* 5.1; Table 1). Otherwise, only the most stable phase (magnesite) would precipitate at 25 °C. Hence, nesquehonite was considered at 25 °C. At a higher temperature, as other Mg-carbonates precipitated (Table 1), hydromagnesite and magnesite were respectively considered at 70 and 90 °C. Initial areas of the mineral were adjusted to fit the observed experimental data (aqueous Mg and Ca concentrations). The composition of the initial solution was that of the input solution.

4.2 Thermodynamic and kinetic data

Eleven species in solution and seven (25 °C) and eight minerals (70 and 90 °C) were considered in each calculation depending on the case (Tables 2 and 3). The equilibrium constants for the homogeneous and mineral reactions at 25, 70 and 90 °C listed in Tables 2 and 3 are from the EQ3/6 thermodynamic database (Wolery et al., 1990), which coincide with those provided in the Llnl and Phreeqc databases (Phreeqc v.3; Parkhurst and Appelo, 2013). The effect of pressure on log K_{eq} values was examined for some mineral reactions (calcite, dolomite, quartz and aragonite) using Phreeqc v.3 and Phreeqc database. The resulting variation in the log K_{eq} values between 10 and 50 bar was less than 0.5% and less than 0.7% between 10 and 74 bar, yielding a marginal P effect on the log K_{eq} values in the pressure range of this study. Therefore it was assumed that uncertainties originated by the CrunchFlow calculations, which do not take into account the pressure effect on the log K_{eq} values for homogeneous and mineral reactions, are likely to be marginal. Solubilities of CO$_2$ at high P were implemented by

fixing the activities of $CO_{2(aq)}$ (equilibrium $CO_{2(g)} \Leftrightarrow CO_{2(aq)}$) to the solubility calculated from the model by Duan and Sun (2003) at each pCO_2 and T at zero ionic strength (Table 4). The activity coefficients were calculated using the extended Debye-Hückel formulation (b-dot model; Helgeson, 1969).

The kinetic rate laws for the reacting minerals (Eqs. (7) and (8)) used in the present study were obtained from Bullard et al. (2010) for portlandite and from Cubillas et al. (2005) for aragonite. The kinetic rate laws for nesquehonite and hydromagnesite, which were assumed to be the same as magnesite, and for the other minerals were from Palandri and Kharaka (2004; Table 5). The rate laws used basically account for mineral dissolution. Since the kinetics of mineral precipitation is generally unknown, and considering that precipitation occurs near equilibrium, the dissolution rate laws were assumed to be a proxy for the precipitation kinetics. A crucial parameter to fit models to experimental data using reactive transport codes is the value of the reactive surface area of primary minerals (A_r in $m^2_{mineral}$ m^{-3}_{bulk}). Using the specific surface area of the initial solid (A_{BET} in $m^2_{mineral}$ g^{-1}) and the bulk volume (V_{bulk} in m^3), a resulting total surface area of 5.1×10^5 $m^2_{mineral}$ m^{-3}_{bulk} was calculated ($A_r = A_{BET}.m_{MgO}/V_{bulk}$; m_{MgO} = sample mass (g)). The reactive surface area calculated assuming spherical geometry was 6×10^3 $m^2_{mineral}$ m^{-3}_{bulk} which differs in 2 orders of magnitude from the BET value. However, to match the experimental results a smaller value had to be given (average of 1.1×10^5 $m^2_{mineral}$ m^{-3}_{bulk}) (Table 6). Surface areas of secondary minerals (except dolomite) had to be sufficiently large to facilitate their precipitation. Initial surface area for Mg-carbonates was calculated from the total area (1.1×10^5 $m^2_{mineral}$ m^{-3}_{bulk} in average) multiplied by initial volume fraction.

5. Results and discussion

5.1 Experimental results

XRD-Rietveld analyses of the solids in the different experiments showed that with increasing temperature the secondary Mg carbonate phases that tended to precipitate are less hydrated (Table 1). Bénézeth et al. (2011) showed the chemical composition of the different phases crystallizing in the system $MgO–CO_2–H_2O$. The results of the present study coincide with their results. The less stable Mg-carbonate phases are those with a higher content of water and tend to form at a low temperature. Hänchen et al. (2008)

and Kristova et al. (2014) reported that metastable Mg-carbonate phases are progressively replaced by more stable ones.

SEM images of the initial sample show the common morphology of MgO grains (Fig 2a). At 25 °C, based on crystal morphology, precipitation of nesquehonite (well-formed needles) was observed in the samples reacted at pCO_2 of 10 and 50 bar (Fig. 2b). At 70 °C, precipitation of hydromagnesite (thin platelets) dominated (Fig. 2c), and precipitation of magnesite (hexagonal prisms) was enhanced by temperature and pCO_2 (Fig. 2d). Transformation from nesquehonite to hydromagnesite and magnesite with temperature has been observed at 50 and 70 °C and pCO_2 of 82 bar (Schaef et al., 2011) and at 120 °C and pCO_2 of 3 bar (Hänchen et al., 2008). Also, formation of minor amounts of aragonite is measured by XRD-Rietveld analysis (*wt.*% < 7; Table 1). Nonetheless, this phase could not be observed by SEM.

Fig. 3a-d shows variation of concentration of Mg and Ca over time in the experiments at subcritical pCO_2 of 10 and 50 bar and 25, 70 and 90 °C. Note that Mg concentration was more than one order of magnitude higher than that of calcium because of the higher $Mg(OH)_2$ content compared to that of $CaCO_3$ and $Ca(OH)_2$. Variation in Mg concentration was similar at pCO_2 of 10 and 50 bar. At both values of pCO_2, Mg and Ca release tended to be higher at 25 than at 70 and 90 °C. Over time Mg and Ca concentration tended to reach steady state at three temperatures. In the early stages of the experiments, the increase in Mg concentration was assumed to be due to dissolution of brucite whereas the increase in Ca was possibly related to the calcite and portlandite dissolution. Both decreases in their concentrations were assumed to be caused by precipitation of Mg and/or Ca carbonates.

Fig. 3e and f shows variation in concentration of Mg and Ca with time in the supercritical CO_2 experiments (pCO_2 = 74 bar and 70 and 90 °C). The same behavior in Mg concentration was observed as during subcritical CO_2 experiments, with similar Mg concentration. Mg and Ca release tended to be higher at 70 than at 90 °C. Likewise, increase in Mg and Ca concentrations was due to dissolution of brucite, calcite and portlandite, whereas decrease in their concentrations was caused by precipitation of Mg and/or Ca carbonates. At 90°C, the Ca concentration started to increase after reaching an early plateau, probably caused by a faster dissolution of the Ca-bearing phases in the absence of Mg (Fig.3f). The experimental results were compared under subcritical and

supercritical CO_2 conditions: at 70 °C, an increase in pCO_2 resulted in a very slight increase in Mg concentrations, whereas at 90 °C, they were similar (≈ 4.0×10^{-2} mol kgw^{-1}; (Fig. 3a,c,e); at 70 °C, the Ca concentration increased to reach a maximum value between 1 and 9 h after the start, tending to remain steady thereafter (Fig. 3b,d,f). At 90 °C, the variation in Ca concentration was similar except under supercritical CO_2 conditions in which tended to increase.

5.2 Modeling results

Reasonable fits for the aqueous Mg and Ca concentrations were achieved under the different pCO_2 and temperature conditions (Fig. 3), leading to an interpretation of the evolution of the overall MgO carbonation process. Table 6 lists the minerals considered in the modelling under the different pCO_2 and T conditions. Fig. 3a and b shows the simulated variation in Mg and Ca concentration at pCO_2 of 10 bar. To match the Mg experimental variation with time, dissolution of brucite, precipitation of dolomite (25, 70 and 90 °C), nesquehonite (25 °C) and both hydromagnesite and magnesite (70 and 90 °C) were considered. The Ca experimental variation was matched by considering significant dissolution of portlandite that increased the Ca release and the solution saturation with respect to calcite and dolomite, promoting calcite precipitation at 25 °C and dolomite at 25, 70 and 90 °C. Likewise, at pCO_2 of 50 bar, the same processes occurred. However, magnesite precipitation ought to be considered to match the Mg experimental variation at 25 °C, even though this Mg-carbonate phase is more stable at higher temperatures as observed in this study and reported in the literature (e.g., Unluer and Tabbaa (2013); Sim. B; Fig. 3c and d). Dissolution of portlandite and calcite (70 and 90 °C) and precipitation of calcite (25 °C) and dolomite (25, 70 and 90 °C) were taken into account to match the experimental Ca variation (Fig. 3c and d).

Under supercritical pCO_2 conditions, the same processes as those at 50 bar were taken into account to match the Mg experimental variation at 70 and 90 °C. Dissolution of brucite and precipitation of dolomite, hydromagnesite and magnesite were considered to match the Mg experimental variation. With respect to Ca, dissolution of portlandite and calcite was considered (Fig. 3e and f).

A match between the simulated and experimental changes of Mg and Ca concentrations with time and the final mineral volume fraction (Fig. 3) was achieved by adjusting the mineral reactive surface areas at 10, 50 and 74 bar. At 25 °C and 10 and 50 bar, the

simulated Mg concentration could not match a faster precipitation of the secondary phases observed by the experimental concentration. The fitted values of the brucite reactive surface areas were decreased with temperatures from $3.2 \pm 0.3 \times 10^{2}$ $m^{2}_{mineral}$ mol^{-1} (25 °C) to $4.2 \pm 3.0 \times 10^{3}$ $m^{2}_{mineral}$ mol^{-1} (70 and 90 °C; Table 6) to slow down the brucite's dissolution rates, i.e., to reduce its reactivity. This decrease could be likely caused by formation of Mg-carbonate coatings over the $Mg(OH)_2$ grains, causing passivation (Harrison et al., 2015). Moreover, at the higher temperatures precipitation rates of hydromagnesite and magnesite started at the onset of the experiments in contrast to that of nesquehonite that started at about 40 h at low temperature (Fig. S2, Supplementary data). Therefore, it was deduced that passivation of $Mg(OH)_2$ was likely stronger at high temperature. In the case of Ca variation, the reactive surface area of calcite was $1.1 \pm 0.9 \times 10^{1}$ $m^{2}_{mineral}$ mol^{-1} at 10 bar and smaller at 50 and 74 bar ($2.8 \pm 4.0 \times 10^{-1}$ $m^{2}_{mineral}$ mol^{-1}). The ΔG_r dependence of the calcite dissolution rate in the model was taken from Xu et al. (2012), but they did not have experimental data in this range of ΔG_r values (Eq. 8). As a result, the calcite dissolution rate law may overestimate the dissolution rate in this ΔG_r range, and hence a lower surface area is necessary. The reactive surface area of dolomite was rather small, ranging from $1.1 \pm 0.7 \times 10^{-7}$ to $7.2 \pm 2.0 \times 10^{-6}$ $m^{2}_{mineral}$ mol^{-1}. This variability was associated to the very small content of dolomite (*vol.*% < 0.6). Also, variability in the reactive surface of portlandite ($3.2 \pm 0.1 \times 10^{-5}$ to $5.7 \pm 1.3 \times 10^{-1}$ $m^{2}_{mineral}$ mol^{-1}) was attributed to its small content (*vol.*% <3). The reactive surface of quartz was the same over the whole temperature range because its dissolution was very slight. Regarding the secondary Mg-bearing minerals, the reactive surface area of nesquehonite was the same in all the experiments at 25 °C (Table 6). In the case of hydromagnesite, the reactive surface area was $2.0 \pm 1.3 \times 10^{-3}$ $m^{2}_{mineral}$ mol^{-1} over the pCO_2 and temperature ranges of this study. As for magnesite, at 10 bar and 70-90 °C the reactive surface area was a factor of 0.01 lower than that of hydromagnesite. By increasing pCO_2 and temperature (50 and 74 bar and 70-90 °C), magnesite was the most stable Mg-carbonate phase, thus dominating the overall precipitation. In this case, the reactive surface area increased to match the variation in Mg concentration and Mg-mineral volumetric fraction (Tables 6 and 7). This suggests that the increase in reactive surface area with increasing temperature is related to distinct growth and nucleation of magnesite, which are difficult to predict. The large surface area for nesquehonite at 25 °C indicates that this phase precipitates

under or near local equilibrium conditions (only limited by the dissolution rate of the primary minerals) instead of occurring as heterogeneous nucleation that could originate under non-stirring conditions. The small amount of precipitated aragonite (*vol.*% between 2 and 7 %) could not be reproduced by the model.

Fig. 4 shows the calculated variation of pH throughout the experiments. Overall, pH increased as brucite dissolved and CO_2 solubility increased by decreasing T (Table 4), buffering the pH. Thereafter steady state was achieved under both subcritical and supercritical pCO_2 conditions. Independently of pCO_2, pH was higher at 25 °C than at 70 and 90 °C because brucite dissolution rate (R_m) was greater at the lowest temperature as is shown in Fig. S2 (supplementary data). Although the brucite dissolution rate constant increases with temperature ($k_{m,T}$ = 1.86 × 10^{-5}, 4.22 × 10^{-4} and 1.32 × 10^{-3} mol m^2 s^{-1} at 25, 70 and 90 °C, respectively), $f_m(\Delta G_r)$ in Eq. (8) decreases as IAP/K_{eq} increases (lower $SI_{Brucite}$ at 25 than at 90 °C; see Fig. S1, supplementary data), yielding slower brucite dissolution rate (R_m) at high temperature.

At pCO_2 of 10 bar and 25 °C, the solution was undersaturated with respect to brucite all over the experiment (Fig. S1, supplementary data), corroborating $Mg(OH)_2$ dissolution. This yielded an increase in Mg concentration and a consequent supersaturation with respect to dolomite and nesquehonite (positive *SI* values) after ca. 10 h and 40 h, respectively. As a consequence, Mg concentration reached steady state (Fig. 3a), which lasted until brucite started to run out, and the rates of brucite dissolution and nesquehonite precipitation decreased (Fig. S2, supplementary data). The solution was undersaturated with respect to both calcite and portlandite in the first 10 h (Fig. S1, supplementary data), yielding an increase in Ca concentration. Thereafter, when pH was about 6.2 the solution became supersaturated with respect to calcite and dolomite but still remained undersaturated with respect to $Ca(OH)_2$. Also, steady state of Ca concentration was reached (Fig. 3b), and it lasted until portlandite started to exhaust (i.e., portlandite dissolution rate decreased rapidly; Fig. S2, supplementary data). At higher temperatures, *SI* with respect to brucite was higher than at 25 °C throughout the experiment, but still negative, also yielding an increase in Mg concentration and consequent supersaturation with respect to dolomite after ca. 10 h. Nonetheless, the nesquehonite *SI* showed undersaturation during the experiments. Solution was always supersaturated with respect to hydromagnesite and magnesite over the whole temperature range andundersaturated with respect to calcite and portlandite (Fig. S1,

supplementary data). As in the case of 10 bar of pCO_2, at 50 and 74 bar, the calculated solution saturation state with respect to brucite, calcite, dolomite, portlandite and quartz was similar (Fig. S3 and S4, supplementary data). Regarding the Mg-carbonate phases, the solution was always undersaturated with respect to nesquehonite and hydromagnesite, while it became quickly supersaturated with respect to magnesite.

Variation of the mineral volume fractions over time under the different pCO_2 conditions is shown in Figs. 5, 6 and 7. At 10 bar (Fig. 5), brucite dissolved with time at all temperatures (e.g., 95 % at 25 °C; Fig. 5a). The temperature increase reduced brucite dissolution. Precipitation of calcite only took place at 25 °C, (Fig. 5b). Portlandite dissolution occurred at all temperatures, being greater at 25 °C (Fig. 5c), in accordance with the log K_{eq} (Table 3) and also the solution saturation state (*SI*; Fig. S1, supplementary data). Quartz dissolution was negligible (Fig. 5d). Dolomite precipitation occurred at high temperature, becoming greater at 90 °C (Fig. 5e) and leaving a higher Ca concentration at 25 °C, resulting in a supersaturated solution with respect to calcite (Fig. S1, supplementary data). Regarding the Mg-carbonates, nesquehonite precipitated at 25 °C and precipitation of hydromagnesite and magnesite took place at 70 and 90 °C (Fig. 5f).

At pCO_2 of 50 and 74 bar, brucite and portlandite also tended to dissolve, and quartz dissolution was also insignificant. Dolomite precipitation also occurred at high temperature. Calcite precipitated at 25 °C and pCO_2 of 50 bar but dissolved at higher temperature (Fig. 6a,b). At pCO_2 of 50 bar, nesquehonite did not precipitate at 25 °C. At higher temperature hydromagnesite and magnesite precipitation was favored (Fig. 6c). At pCO_2 of 74 bar, precipitation of hydromagnesite and magnesite also occurred but the volume of Mg-carbonate was higher at 90 °C than at 70 °C (Fig. 6d).

The initial porosity ($\phi_{(i)}$) was calculated dividing the pore volume ($V_{solution}$) by the total volume ($V_{solution}$ + V_{solid}). In the model the porosity evolves as the mineral volume fractions evolve, yielding a final porosity ($\phi_{(f)}$). Variation in porosity ($\phi_{(f)}$ - $\phi_{(i)}$) normalized with respect to the initial total mineral *vol.%* (1 - $\phi_{(i)}$) is shown in Fig. 7. At pCO_2 of 10 and 50 bar, porosity was higher at 25 °C than at higher temperature. At 10 bar and 25 °C, porosity gradually increased, but thereafter decreased because nesquehonite precipitation took place. By contrast, porosity gradually increased at pCO_2 of 50 bar owing to the lack of nesquehonite precipitation. At pCO_2 of 74 bar

(supercritical CO_2 conditions), porosity was higher at 70 than at 90 °C. A final overall decrease in porosity occurred at 90 °C.

Fig. 8 shows the variation in mineral volume fraction under all pCO_2 conditions and 90 °C. Dissolution of brucite was favored by a pCO_2 increase (Fig. 8a). Likewise, dissolution of calcite and portlandite and precipitation of dolomite were favored by the increase in pCO_2 (Fig. 8b,c,d). Precipitation of hydromagnesite and magnesite was also favored by the increase in pCO_2 (Fig. 8e). The balance between these reactions led to an initial increase in porosity, followed by a gradual decrease, which was greater at lower pCO_2 (Fig . 9).

The comparison between the measured (Exp.) and calculated (Sim.) variation in volume fractions is shown in Table 7. Considering the low values of measured concentrations and the uncertainty associated to the Rietveld analysis, a good match between the calculated and measured values is when the differences are ≤ 7 *vol.*%. The calculations used to convert the mineral *wt.%* obtained from the Rietveld analysis (Table 1) to mineral volume fraction (*vol.%*; Table 7) are given in Appendix A. In general, the calculated mineral volume fractions were in reasonable agreement with the measured ones, and although some discrepancies were found, the major occurring processes were identified (Table 7): at 10 bar (25-70 °C), the mismatch between the calculated volume fraction and the measured one of brucite, hydromagnesite and calcite are between 10-12 *vol.*%. At high pCO_2 (50 and 74 bar), the calculated brucite volumetric fraction is always greater than the simulated one, except for the experiment at 74 bar and 90 °C, where brucite was exhausted. At 50 bar, the calculated volume fractions of calcite (70 °C) and hydromagnesite (90 °C) are lower than the measured ones (10-11 *vol.* %). At 74 bar, the calculated volume fractions of hydromagnesite (70 °C) and magnesite (90 °C) are lower than the measured ones (9-17 *vol.*%). The inference is that discrepancies are to be expected since experimental nucleation of precipitated Mg-bearing minerals is hardly quantifiable, and small changes in reactive surface area originate large variation in the mineral volumetric fraction. In addition, it is notable that at 50 bar and 25 °C the measured nesquehonite volume fraction could not be reproduced at all, suggesting only possible uncertainty in the log K_{eq} for nesquehonite and its dependence on P.

The experimental and modeling results using MgO (as a representative of a MgO-based cement) show that MgO has a self-healing tendency promoted by precipitation of Mg-

carbonates under subcritical and supercritical CO_2 conditions. This behavior is also observed in experimental and field studies using Portland cement (Carey, 2013), in which a substantial self-healing tendency arises not only from precipitation of Ca-carbonates but also originates from swelling of Ca-depleted residual C-S-H phases and reprecipitation of cement phases. Compared to Portland cements that provide a highly alkaline environment that passivates the surface of steel (Carey, 2013), the performance of MgO-based cements within this respect is unclear. Ultimately, the properties of Portland cement depend highly on the water/cement ratio, which may be also a critical factor for the MgO-based cement properties.

5.3 Application case: borehole-cement-reservoir rock interface

The geological sequestration of CO_2 involves injection through wells. Usually, boreholes are surrounded by a layer of Portland cement mortar (Carey et al., 2007; Duguid et al., 2011; Scherer et al., 2011). In this work, MgO-based cement is studied as an alternative to Portland cement. This section intends to illustrate how the interaction between CO_2-rich water and the Mg-based cement surrounding the well at deep levels could occur. This scenario assumes a leak in the well casing causing diffusive exchange between the CO_2-rich water in the borehole, the Mg-based cement and eventually the limestone reservoir rock (Fig. 10). This process could induce changes in the composition of the original MgO-based cement mainly due to brucite dissolution and magnesite precipitation and cause variation in its porosity and sealing capacity. Note that in this application case the set of hypotheses presented represents general conditions to the point where more realistic conditions would be necessary to model any real case (e.g., crack dimensions, injection parameters, wellbore features, precise depth, etc.).

1-D modeling with symmetry around the borehole axis was performed assuming that solute transport is dominated by diffusion perpendicular from the well to the reservoir rock. A single value of diffusion coefficient in water (D_o) was used to calculate the effective diffusion coefficients for all species as the aqueous solution is mainly composed of Mg^{2+} and Ca^{2+} ions. Effective diffusion coefficients in the model were calculated from $D_{eff} = \phi\alpha D_o$, where ϕ is porosity, α is a lithology factor and D_o equals 4.5×10^{-9} m^{-2} s^{-1} at 90 °C (Samson et al., 2003). The initial effective diffusion coefficient (D_{eff}) was assumed to be 1.13×10^{-11} m^2 s^{-1}, which is a value in the range for

Portland cement grouts (Laurila et al., 2005; Soler et al., 2010; 2011). Nonetheless, a sensitivity analysis was carried out assuming that the initial effective diffusion coefficient in the cement ranged from 1.13×10^{-12} to 1.13×10^{-10} m^2s^{-1} (Table 8). D_e in the model changes linearly with porosity.

Details of the spatial discretization are given in Table 9. Initial porosities of the MgO-based cement and the reservoir rock are 0.5 (50%; Taylor, 1997) and 0.1 (10%; Noiriel et al., 2005), respectively. The initial water in the MgO-based cement is water at atmospheric conditions with pH of 5.82 (Table 10). The initial composition of porewater in the reservoir rock is at equilibrium with respect to calcite and dolomite with a pH of 7.5 (Table 10). The CO_2-rich water is assumed to be at 150 bar and 90 °C (e.g., at supercritical CO_2 conditions), yielding a pH of 3.17 (Table 10). The values of the mineral surface areas of the MgO-based cement are those obtained from the laboratory simulations (Table 6), and the values in the rock are considered generally close enough to local equilibrium to allow dissolution (8.6×10^6 $m^2_{mineral}$ m^{-3}_{bulk}).

The pH variation with distance from the borehole to the reservoir rock is shown in Fig. 11a. In the borehole, the CO_2-rich water at pCO_2 of 150 bar and 90 °C has a constant pH of 3.17. Fast equilibration of the cement porewater with brucite and portlandite causes a fast initial increase in pH to values close to 9. Diffusive exchange with the CO_2-rich water in the borehole causes a gradual decrease in the pH of the cement porewater (Fig. 11b). The composition of the reservoir rock porewater is disturbed up to a distance of 7 m from the borehole after 300 y (Fig. 11a) with the hypotheses of the modelling, i.e. a very simple chemical and mineralogical system.

As the CO_2-rich water interacts with the cement, a front originates in which porosity decreases from 50 % to ca. 41 % (Fig. 11c) as a result of magnesite precipitation induced by the dissolution of brucite. Notice also the advance of a high-porosity front starting at the borehole-cement interface, especially after 150 y (Fig. 11c). The advance of this front is caused by the dissolution of magnesite in contact with the CO_2-rich water in the borehole (Fig. S5; supplementary data).

Over time, precipitation of dolomite at the cement-rock interface results in the complete sealing of porosity at the interface (t ca. 200 y; Fig. 11d). Dolomite precipitation is caused by the dissolution of magnesite (cement side of the interface) and calcite (rock side of the interface). The sealing of porosity would be beneficial for the isolating

properties of the cement. On the rock side of the interface porosity increases from 10 to 18 % (~ 0.18 m), due to the dissolution of calcite.

A limited sensitivity analysis (Fig. 12) was performed by changing the initial effective diffusion coefficient (D_{eff}) of the cement to one order of magnitude smaller (1.13×10^{-12} m^2 s^{-1}) and larger (1.13×10^{-10} m^2 s^{-1}) values. It is inferred that with the larger value of D_{eff}, the fast advance of the high-porosity front would be highly detrimental for the performance of the cement.

6. Conclusions

Stirred batch experiments conducted at different pCO_2 and temperature (10, 50 and 74 bar and 25, 70 and 90 °C) were useful to study the evolution of MgO carbonation, which involves the fast hydration of MgO to brucite, the dissolution of brucite and the precipitation of magnesium carbonates. Numerical simulations of the experimental results allow quantification of the overall process. Together these procedures shed light on the potential application of MgO-based cement as alternative cement in a context of CO_2 sequestration.

An increase in pCO_2 favors brucite dissolution, promoting formation of magnesium carbonates. At 10, 50 and 74 bar, increasing temperature hydrated Mg-carbonates (nesquehonite) transformed into those that are less hydrated (hydromagnesite and magnesite). Calcite, portlandite and quartz dissolution and dolomite and calcite precipitation are only minor. The balance between these reactions leads to a decrease in porosity by increasing temperature and decreasing pCO_2.

Initial values of the reactive surface areas of primary and secondary minerals were adjusted in order to numerically reproduce the experimental results. However, at 25 °C and 50 bar, nesquehonite (observed by XRD in the precipitates) was not calculated to precipitate. Fitting the model of aqueous Mg concentration and mineral volume fractions involved the use of large surface area for nesquehonite (25 °C) indicating that this phase precipitates under or near local equilibrium conditions (only limited by the dissolution rate of the primary minerals). Dolomite precipitation is always strongly inhibited.

Based on the assumptions presented in this study, simulations of an application case over 300 years in a limestone reservoir rock borehole show that brucite dissolution and

magnesite precipitation lead to a decrease of the initial porosity of the cement from 50 to 42 %. Additionally, magnesite precipitation at the cement-rock interface leads to the sealing of porosity. These decreases in porosity would be beneficial for the performance of the cement. However, fast dissolution of magnesite at the contact with the borehole was calculated for the case with a largely effective diffusion coefficient, which would be detrimental for performance under those conditions.

Future research should contemplate the performance of coreflood experiments to completely characterize the interaction between the well casing and the MgO-based cement under different *P* and *T* conditions related to CO_2 injection, as well as the effect of impurities in the gas.

Acknowledgements

This work was funded by project ALM/11/009 of the Fundación Ciudad de la Energía (CIUDEN), project CICYT-OXYCFB300 of the Spanish Government, project 2014SGR (Grup de Recerca SGR) 1456 of the Catalan Government and by the European Union through the "European Energy Programme for Recovery", the Compostilla OXYCFB300 project and by two European projects, the MUSTANG project (European Community's Seventh Framework Programme FP7/2007-2013 under grant agreement number 227286) and the PANACEA project (European Community's Seventh Framework Programme FP7/2007-2013 under grant agreement number 282900). GD is supported by a JAE-Predoc grant under the Program "Junta para la Ampliación de Estudios". LL is supported by a Juan de la Cierva postdoctoral grant (MINECO, Spain). We would like to thank Natàlia Moreno (IDAEA), Eva Pelegrí and Maite Romero (SCT-Barcelona University) and Alejandro Blanco and Jordi Bellés (IDAEA) for analytical assistance. We also wish to thank two anonymous reviewers for their constructive comments that have improved the quality of the paper.

Appendix A

The mineral content expressed as percentage by mass (*wt.%*) obtained from the Rietveld analysis (Table 1) has been calculated as percentage by volume (*vol.%*; Table 7) using the following expressions:

$$vol.\% = \frac{vol_m}{vol_T} \quad \text{(A1)}$$

where vol_T is the total volume expressed as

$$vol_T = \sum_m vol_m \quad \text{(A2)}$$

and vol_m is the volume of mineral m calculated as

$$vol_m = \frac{m_m}{\rho_m} \quad \text{(A3)}$$

where m_m is the mass of mineral

$$m_m = m_T \cdot wt.\% \quad \text{(A4)}$$

and m_T and ρ_m are the sample mass and the mineral density, respectively.

Appendix B Supplementary data

Figure captions

Figure S1. Variation of the simulated saturation index (SI_m) of minerals (brucite, calcite, portlandite, quartz, dolomite, nesquehonite, hydromagnesite and magnesite) as a function of time at 25, 70 and 90 °C and $p\mathrm{CO_2}$ = 10 bar.

Figure S2. Variation of the simulated mineral dissolution/precipitation rates (R_m) (brucite, calcite, portlandite, quartz, dolomite, nesquehonite, hydromagnesite and magnesite) as a function of time at 25, 70 and 90 °C and $p\mathrm{CO_2}$ = 10 bar.

Figure S3. Variation of the simulated saturation index (SI_m) of minerals (brucite, calcite, dolomite, nesquehonite, hydromagnesite and magnesite) as a function of time at 25, 70 and 90 °C and $p\mathrm{CO_2}$ = 50 bar.

Figure S4. Variation of the simulated saturation index (SI_m) of minerals (brucite, calcite, dolomite, nesquehonite, hydromagnesite and magnesite) as a function of time at 25, 70 and 90 °C and $p\mathrm{CO_2}$ = 74 bar.

Figure S5. Simulated variation of the mineral dissolution/precipitation rates (R_m) at the borehole-cement interface: borehole from 0 to0.11 m; MgO-based cement from 0.11 to 0.18 m and reservoir rock from 0.18 to 7.01 m.

References

Abdoulghafour, H., Luquot, L., Gouze, P., 2013. Characterization of the Mechanisms Controlling the Permeability Changes of Fractured Cements Flowed Through by CO_2-Rich Brine. Environ. Sci. Technol. 47, 10332–10338.

Bachu, S., Bennion, D.B., 2009. Experimental assessment of brine and/or CO_2 leakage through well cements at reservoir conditions. Int. J. Greenh. Gas Con. 3, 494–501.

Back, M., Bauer, M., Stanjek, H., Peiffer, S., 2011. Sequestration of CO_2 after reaction with alkaline earth metal oxides CaO and MgO. Appl. Geochem. 26, 1097–1107.

Bénézeth, P., Saldi, G.D., Dandurand, J.L., Schott, J., 2011. Experimental determination of the solubility product of magnesite at 50 to 200 °C. Chem. Geol. 286, 21–31.

Bullard, J.W., Enjolras, E., George, W.L., Satterfield, S.G., Terrill., J.E., 2010. A parallel reaction-transport model applied to cement hydration and microstructure development. Modelling Simul. Mater. Sci. Eng., 18, 16.

Carey, J.W., 2013. Geochemistry of wellbore integrity in CO_2 sequestration: Portland cement-steel-brine-CO_2 interactions. Rev. Mineral Geochem. 77, 505–539.

Carey, J.W., Wigand, M., Chipera, S.J., Wolde, G., Pawar, R., Lichtner, P.C., Wehner, S.C., Raines, M.A., Guthrie Jr., G.D., 2007. Analysis and performance of oil well cement with 30 years of CO_2 exposure from the SACROC Unit, West Texas, USA. Int. J. Greenh. Gas Con. 1, 75–85.

Carroll, S.A., McNab, W.W., Torres, S.C., 2011. Experimental Study of Cement−Sandstone/Shale−Brine−CO_2 Interactions. Geochemical Transactions 12, 9.

Celia, M.A., Bachu, S., Nordbotten, J.M., Gasda, S.E., Dahle, H.K., 2005. Quantitative estimation of CO_2 leakage from geological storage: analytical models, numerical models, and data needs, in: Rubin, E.S., Keith, D.W., Gilboy, C.F. (Eds.), Greenhouse Gas Control Technologies, Vol. I, Elsevier, pp. 663–671.

Cubillas, P., Prieto, M., ChaRrat, C., Oelkers, E.H., Kfhler, S., 2005. Experimental determination of the dissolution rates of calcite, aragonite, and bivalves. Chem. Geol. 216, 59–77.

Dávila, G., Garcia-Rios, M., Soler, J.M., Cama, J., 2011. Modeling the dissolution of calcite coupled to gypsum precipitation in acid brines. (Oral). European Geosciences Union General Assembly 2011. Vienna (Austria), April 3-8, in: Geophysical Research Abstracts Vol. 13, EGU2011-716.

Dávila, G., Luquot, L., Soler, J.M., Cama, J., 2015. Interaction between a fractured marl caprock and CO_2-rich sulfate solution under supercritical CO_2 conditions. Int. J. Greenh. Gas Con. doi: 10.1016/j.ijggc.2015.11.005.

Dewaele, P.J., Reardon, E.J., Dayal, R., 1991. Permeability and porosity changes associated with cement grout carbonation. Cem. Con. Res. 21, 441–454.

Duan, Z., Sun, R., 2003. An improved model calculating CO_2 solubility in pure water and aqueous NaCl solutions from 273 to 533 K and from 0 to 2000 bar. Chem. Geol. 193, 257–271.

Duguid, A., 2009. An estimate of the time to degrade the cement sheath in a well exposed to carbonated brine. Energy Procedia 1, 3181–3188.

Duguid, A., Radonjic, M., Scherer, G.W., 2011. Degradation of cement at the reservoir/cement interface from ex`posure to carbonated brine. Int. J. Greenh. Gas Con. 5, 1413–1428.

Ferrini, V., De Vito, C., Mignardi, S., 2009. Synthesis of nesquehonite by reaction of gaseous CO_2 with Mg chloride solution: Its potential role in the sequestration of carbon dioxide. J. Haz. Mat. 168, 832–837.

Fruhwirth, O., Herzog, G.W., Hollerer, I., Rachetti, A., 1985. Dissolution and hydration kinetics of MgO. Surf. Technol. 24, 301–317.

Gasda S.E., Bachu, S., Celia, M.A., 2004. Spatial characterization of the location of potentially leaky wells penetrating a deep saline aquifer in a mature sedimentary basin. Environ. Geol. 46, 707-720.

Gautier, Q., Benezeth, P., Mavromatis, M., Schott, J., 2014. Hydromagnesite solubility product and growth kinetics in aqueous solution from 25 to 75 °C. Geochim. Cosmochim. Acta 138, 1–20.

Hänchen, M., Prigiobbe, V., Baciocchi, R., Mazzotti, M., 2008. Precipitation in the Mg-carbonate system-effects of temperature and CO_2 pressure. Chem. Eng. Sci. 63, 1012–1028.

Harrison, A.L., Dipple, G.M., Power, I.M., Mayer, K.U., 2015. Influence of surface passivation and water content on mineral reactions in unsaturated porous media: Implications for brucite carbonation and CO_2 sequestration. Geochim. Cosmochim. Acta 148, 477–495.

Harrison, J., 2001. Reactive magnesium oxide cements. In: W.I.P. Organisation (Ed.), Australia.

Helgeson, H.C., 1969. Thermodynamics model of hydrothermal systems at elevated temperatures and pressures. Am. J. Sci. 267, 729–804.

Jacquemet, N., Pironon, J., Lagneau, V., Saint-Marc, J., 2012. Armouring of well cement in H_2S–CO_2 saturated brine by calcite coating – Experiments and numerical modelling: Appl. Geoch. 27, 782–795.

Jung, H.B., Kabilan, S., Carson, J.P., Kuprat, A.P., Um, W., Martin, P., Dahl, M., Kafentzis, T., Varga, T., Stephens, S., Arey, B., Carroll, K.C., Bonneville, A., Fernandez, C.A., 2014. Wellbore cement fracture evolution at the cement–basalt caprock interface during geologic carbon sequestration. Appl. Geochem. 47, 1–16.

Kristova, P., Hopkinson, L.J., Rutt, K.J. Hunter, H.M.A., Cressey, G., 2014. Carbonate mineral paragenesis and reaction kinetics in the system MgO–CaO–CO_2–H_2O in presence of chloride or nitrate ions at near surface ambient temperatures. Appl. Geochem. 50, 16–24.

Kutchko, B.G., Strazisar, B.R., Dzombak, D.A., Lowry, G.V.,Thaulow, N., 2007. Degradation of well cement by CO_2 under geologic sequestration conditions. Env. Sci. Technol. 41, 4787–4792.

Kutchko, B.G., Strazisar, B.R., Lowry, G.W., Dzomback, D.A., Thaulow, N., 2008. Rate of CO_2 attack on hydrated Class H well cement under geologic sequestration conditions. Env. Sci. Technol. 42, 6237–6242.

Lasaga, A.C., 1998. Kinetic theory in the earth sciences. Princeton series in geochemistry. Edited by H.D. Holland. Princeton University Press.

Laurila, T., Vuorinen, V., Kivilahti, J.K., 2005. Interfacial reactions between lead-free solders and common base materials. Mater. Sci. Eng. 49, 1–60.

Liteanu, E., Spiers, C.J., 2011. Fracture healing and transport properties of wellbore cement in the presence of supercritical CO_2. Chem. Geol. 281, 195–210.

Luquot, L., Abdoulghafour, H., Gouze, P., 2013. Hydro-dynamically controlled alteration of fractured Portland flowed by CO_2-rich brine cements. Int. J. Greenh. Gas Con. 16, 167–179.

Mo, L., Deng, M., Tang, M., Al-Tabbaa, A., 2014. MgO expansive cement and concrete in China: Past, present and feature. Cement Concrete Res. 57, 1-12.

Nogues, J.P., Nordbottena, J.M., Celia, M.A., 2011. Detecting leakage of brine or CO_2 through abandoned wells in a geological sequestration operation using pressure monitoring wells. Energy Procedia 4, 3620–3627.

Noiriel, C., Bernard, D., Gouze, P., Thibault, X., 2005. Hydraulic properties and micro-geometry evolution accompanying limestone dissolution by acidic water. Oil Gas Sci. Technol. 60, 177–192.

O'Connor, W.K., Dahlin, D.C., Dahlin, C.L., Collins, W.K., 2001. Carbon dioxide sequestration by direct mineral carbonation: Process mineralogy of feed and products. Preprint, 2001 SME Annual Meeting & Exhibit, February 26-28, Denver, Colorado. DOE/ARC-2001-027.

Palandri, J.L., Kharaka, Y.K., 2004. A compilation of rate parameters of water–mineral interaction kinetics for application to geochemical modeling. Science for a Changing World. U.S. Geol. Surv. Open File Report 2004-1068, pp. 64.

Pokrovsky, O.S., Schott, J., 1999. Processes at the magnesium-bearing carbonates/solution interface. II. Kinetics and mechanism of magnesite dissolution. Geochim. Cosmochim. Acta 6, 881– 897.

Rahman, M., Mansur, M.A., Chua, K.H., 1988. Evaluation of advanced cementitious composites for machine tool structures, Annals of the CIRP Annals Manufacturing Technology 37, 373–376.

Samson, E., Marchand, J., 2003. Calculation of ionic diffusion coefficients on the basis of migration test results. Mater. Structu. 36, 156-165.

Sayles, F.L., Fyfe, W.S., 1973. Crystallization of magnesite from aqueous solution. Geochim. Cosmochim. Acta 37, 87–99.

Schaef, H.T, Windisch Jr, C.F, Mc Grail, B. P., Martin, P.F, Rosso, K.M., 2011. Brucite [$Mg(OH)_2$] carbonation in wet supercritical CO_2: An in situ high pressure X-ray diffraction study. Geochim. Cosmochim. Acta 75, 7458–7471.

Schaef, H.T., Windisch Jr., C.F., Mc Grail, B.P., Martin, P.F., Rosso K.M., 2011. Brucite [Mg(OH)] carbonation in wet supercritical CO_2: An in situ high pressure X-ray diffraction study. Geochim. Cosmochim. Acta 75, 7458–7471.

Scherer, G.W., Celia, M.A., Prévost, J.-H., Bachu, S., Bruant, R., Duguid, A., Fuller, R., Gasda, S.E., Radonjic, M., Vichit-Vadakan, W., 2005: Leakage of CO_2 through abandoned wells: role of corrosion of cement, in: Thomas, D.C., Benson, S.M. (Eds.), Carbon Dioxide Capture for Storage in Deep Geologic Formations, Vol. 2, pp. 827-848.

Scherer, G.W., Kutchko, B., Thaulow, N., Duguid, A., Mook, B., 2011. Characterization of cement from a well at Teapot Dome Oil Field: Implications for geological sequestration. Int. J. Greenh. Gas Con. 5, 115–124.

Soler, J. M., Vuorio, M., Hautojärvi, A., 2011. Reactive transport modeling of the interaction between water and a cementitious grout in a fractured rock. Application to ONKALO (Finland). Appl. Geoch. 26, 1115–1129.

Soler, J.M., Mäder, U.K., 2010. Cement-rock interaction: Infiltration of a high-pH solution into a fractured granite core. Geo. Acta 3, 221–233.

Steefel, C.I., Appelo, C.A.J., Arora, B., Jacques, D., Kalbacher, T., Kolditz, O., Lagneau, V., Lichtner, P.C., Mayer, K.U., Meeussen, J.C.L., Molins, S., Moulton, D., Shao, H., Šimůnek, J., Spycher, N., Yabusaki, S.B., Yeh, G.T., 2015. Reactive transport codes for subsurface environmental simulation. Computat. Geosci. 19, 445-478.

Taylor, H. F., 1997. Cement chemistry. Thomas Telford.

Unluer, C., Al-Tabbaa A., 2013. Impact of hydrated magnesium carbonate additives on the carbonation of reactive MgO cements. Cement Concrete Res. 54, 87–97.

Watson, T.L., Bachu, S., 2008. Identification of wells with high CO_2-leakage potential in mature oil fields developed for CO_2-enhanced oil recovery. SPE Paper 112924, SPE Improved Oil Recovery Symposium, Apr 19–23, Tulsa, Oklahoma, U.S.A.

Wolery, T.J., Jackson, K.J., Bourcier, W.L., Bruton, C.J., Viani, B.E., Knauss, K.G., Delany, J.M., 1990. Current status of the EQ3/6 software package for geochemical modeling, in: Melchior, C., Bassett, R.L. (Eds.), Chemical Modeling of Aqueous Systems II. Am. Chem. Soc. Symp. Ser, 416, pp.104–116.

Wolf, G.H., Chizmeshya, A.V.G., Diefenbacher, J., McKelvy, M.J., 2004. In situ observation of CO_2 sequestration reactions using a novel microreaction system. Environmental Science & Technology 38, 932–936.

Xu, J., Fan, C., Teng, H.H., 2012. Calcite dissolution kinetics in view of Gibbs free energy, dislocation density, and pCO_2. Chem. Geol. 322–323, 11–18.

Yalcinkaya, T., Radonjic, M., Willson, C., Bachu, S., 2011. Experimental study on a single cement-fracture using CO_2 rich brine. Energy Procedia 4, 5335–5342.

Young, R.A., 1995. The Rietveld method. International Union of Crystallography Monographs on Crystallography, vol. 5. Oxford University Press, USA.

Zhao, L., Sang, L., Chen, J., Ji, J., Teng, H., 2010. Aqueous Carbonation of natural Brucite: Relevance to CO_2 sequestration. Environ. Sci. Technol. 44, 406–411.

Figure captions

Figure 1. Scheme of the experimental setup. The desired pCO_2 (10-50 bar) in the autoclave is obtained by injecting CO_2 from the $CO_{2\ (liquid)}$ bottle (50 bar). Temperature, up to 90 °C, is reached by heating the autoclave.

Figure 2. SEM images of the starting and reacted samples: (a) initial MgO and quartz (Qtz); (b) nesquehonite (Neq), after 72 h at 50 bar and 25 °C; (c) hydromagnesite (Hym), after 31 h at 74 bar and 70 °C and (d) magnesite (Mgs), after 72 h at 50 bar and 90 °C.

Figure 3. Variation of solution composition with time at different temperatures and subcritical pCO_2 of 10 bar (a) [Mg^{+2}] and (b) [Ca^{+2}], 50 bar (c) [Mg^{+2}] and (d) [Ca^{+2}] and 74 bar (e) [Mg^{+2}] and (f) [Ca^{+2}]. Symbols are experimental data and lines correspond to model results.

Figure 4. Simulated pH variation with time at different pCO_2 and temperature. a) 10 bar, b) 50 bar, and c) 74 bar.

Figure 5. Calculated variation of the mineral volume fraction (*vol.*%) with respect to time and *T* at pCO_2 of 10 bar. a) brucite, b) calcite, c) portlandite, d) dolomite e) Mg-carbonates.

Figure 6. Calculated variation of the mineral volume fraction (*vol.*%) with respect to time and *T* at pCO_2 of 50 bar. a) calcite, b) Mg-carbonates, and at pCO_2 of 74 bar c) calcite and d) Mg-carbonates.

Figure 7. Calculated porosity variation with time at different pCO_2 and *T*. a) 10 bar, (b) 50 bar and (c) 74 bar.

Figure 8. Variation of the simulated volume (*vol*.%) of minerals with respect to time at different sub- and sc- pCO_2 at constant temperature of 90 °C a) brucite, b) calcite, c) portlandite, d) dolomite and e) Mg-carbonates.

Figure 9. Simulated normalized porosity (%) variation with time at different sub- and sc- pCO_2 and T = 90 °C.

Figure 10. Schematic representation of the modeled scenario in which CO_2-rich water diffuses through the MgO cement and the reservoir rock. Distances are from the center of the borehole.

Figure 11. Simulations of a) pH variation along the domain (borehole from 0 to 0.11 m, MgO plug cement from 0.11 to 0.18 m and reservoir rock from 0.18 to 7.01 m); b) detailed variation of porosity at the cement/rock interface zones; c) porosity variation from 0.10 to 0.20 m and d) detailed variation of porosity at the interface MgO layer/reservoir rock. Time spans from 1 to 300 years.

Figure 12. Sensitivity analysis on simulations: variation of pH (a) and porosity (b) with distance by changing the effective diffusion coefficient (D_{eff}).

Table headings

Table 1 XRD (Rietveld analyses) of the starting and reacted samples at different *T* and pCO_2.

Table 2 Homogeneous reactions (speciation) considered in the reactive transport model. Reactions are written as the destruction of 1 mole of the species in the first column.

Table 3 Mineral reactions considered in the reactive transport model. Reactions are written as the dissolution of 1 mole of mineral.

Table 4 Concentrations and log activities (fixed) of $CO_{2(aq)}$ (mol kgw^{-1}); *T* = 25, 70 and 90 °C; pCO_2= 10, 50 and 74 bar.

Table 5 Reaction rates and activation energies for the mineral reactions considered in the models. The 2 parallel rate laws for each mineral describe the pH dependencies under different pH ranges.

Table 6 Mineralogical composition and associated surface areas that were used in the simulations.

Table 7 Experimental and simulated reacted volume fraction (*vol.%*) calculated for each experimental conditions.

Table 8 Initial effective diffusion coefficients used for the sensitivity analysis in the simulations.

Table 9 Spatial discretization (number of nodes and grid spacing).

Table 10 Chemical composition (total concentrations and pH) of the initial waters used in the simulations.

Table 1

Sample	**Initial**	**1**	**2**	**3**	**4**	**5**	**6**	**7**	**8**
pCO_2 [bar]	atmospheric	10	10	10	50	50	50	74	74
Temperature [°C]	25	25	70	90	25	70	90	70	90
time [h]	-	74	72	72	72	72	72	72	72
Minerals	***wt.%***								
MgO	**86.9**								
brucite		20.0	3.0	20.0	18.0	0.0	9.0	13.0	0.0
calcite	3.1	17.0	12.0	6.0	5.0	12.0	3.0	8.0	4.0
dolomite	0.6				1.0	1.0	3.0	4.0	1.0
quartz	5.2	4.0	2.0	4.0	6.0	3.0	4.0	4.0	3.0
portlandite	3.1			6.0		4.0	5.0		
nesquehonite		**57.0**		0.0	**68.0**				
hydromagnesite	1.1		**29.0**	**42.0**		**4.0**	**10.0**	**19.0**	
magnesite			**46.0**	**20.0**	2.0	**74.0**	**66.0**	**50.0**	**91.0**
aragonite		2.0	7.0	2.0		1.0		2.0	
others			1.0			1.0			1.0

wt.% = mineral content expressed as percentage by mass
Table 7 shows the mineral content expressed as percentage by volume (*vol.%*)

Table 2

				Stoichiometric coefficients					
species	**log $K_{eq(25°C)}$**	**log $K_{eq(70°C)}$**	**log $K_{eq(90°C)}$**	**Ca^{+2}**	**Mg^{+2}**	**$SiO_{2\,(aq)}$**	**HCO_3^-**	**H^+**	**H_2O**
$CO_{2(aq)}$	-6.34	-6.28	-6.35	0	0	0	1	1	-1
CO_3^{--}	10.33	10.11	10.09	0	0	0	1	-1	0
$CaCO_{3(aq)}$	7.01	6.31	6.07	1	0	0	1	-1	0
$CaHCO_3^+$	-1.04	-1.22	-1.35	1	0	0	1	0	0
$CaOH^+$	12.85	12.85	12.85	1	0	0	0	-1	1
$H_2SiO_4^{--}$	22.96	22.96	22.96	0	0	1	0	-2	2
$HSiO_3^-$	9.94	9.36	9.17	0	0	1	0	-1	1
$Mg_4(OH)_4^{++++}$	39.75	39.75	39.75	0	4	0	0	-4	4
$MgCO_{3(aq)}$	7.36	6.82	6.64	0	1	0	1	-1	0
$MgHCO_3^+$	-1.03	-1.22	-1.36	0	1	0	1	0	0
OH^-	13.99	12.81	12.43	0	0	0	0	-1	1

Table 3

Minerals	log $K_{eq(25°C)}$	log $K_{eq(70°C)}$	log $K_{eq(90°C)}$	Ca^{+2}	Mg^{+2}	$SiO_{2\ (aq)}$	HCO_3^-	H^+	H_2O
brucite	16.30	13.77	12.86	0	1	0	0	-2	2
calcite	1.85	1.19	0.91	1	0	0	1	-1	0
dolomite	2.52	1.00	0.38	1	1	0	2	-2	0
quartz	-4.01	-3.35	-3.16	0	0	1	0	0	0
portlandite	22.56	19.61	18.55	1	0	0	0	-2	2
nesquehonite	4.99	4.67	4.68	0	1	0	1	-1	3
hydromagnesite	30.87	23.78	21.13	0	5	0	4	-6	6
magnesite	2.30	1.21	0.78	0	1	0	1	-1	0
aragonite	2.00	1.33	1.05	1	0	0	1	-1	0

Values of log K_{eq} of magnesite in this study differ from 1 to 3% in this range of temperature with the values reported by Bénézeth et al. (2011)

Table 4

	pCO_2 = 10bar		pCO_2 = 50bar		pCO_2 = 74bar	
Temperature [°C]	**Concentration [mol kgw^{-1}]**	***log (activity)***	**Concentration [mol kgw^{-1}]**	***log (activity)***	**Concentration [mol kgw^{-1}]**	***log (activity)***
25	3.16×10^{-1}	-0.501	1.20×10^{0}	0.078		-
70	1.39×10^{-1}	-0.858	5.95×10^{-1}	-0.226	7.88×10^{-1}	-0.103
90	1.09×10^{-1}	-0.965	4.95×10^{-1}	-0.306	6.70×10^{-1}	-0.174

Table 5

Pressure		**atm**	**atm**		
Temperature		**25 °C**	**25 °C**		
Mineral	$n(a_{H+}^{n})$	$k_{m,25}$ [mol m^{-2} s^{-1}]	Ea [kcal mol^{-1}]	m_1	m_2
brucite	0.5	1.86×10^{-05} 5.75×10^{-09}	14.10 10.04		
calcite	1.0	5.01×10^{-01} 1.55×10^{-06}	3.44 5.62	3.0	1.0
dolomite	0.5	1.74×10^{-04} 2.51×10^{-09}	13.53 22.75		
quartz	0.3	5.01×10^{-15}	15.00		
portlandite	1.0	3.98×10^{-06}	15.0		
nesquehonite	1.0	4.17×10^{-07} 4.57×10^{-10}	3.44 5.61	1.0	4.0
hydromagnesite	1.0	4.17×10^{-07} 4.57×10^{-10}	3.44 5.61	1.0	4.0
magnesite	1.0	4.17×10^{-07} 4.57×10^{-10}	3.44 5.61	1.0	4.0
aragonite	1.0	7.94×10^{-09}	0.00		

See Eqs. (7), (8) and (10) for $n(a_{H+}^{n})$, $k_{m,25}$, Ea, m_1 and m_2
magnesite affinity dependence (Pokrovsky and Schott, 1999)
calcite affinity dependence (Xu et al., 2012)

Table 6

pCO_2 [bar]			10	10	10	50	50	50	74	74
T [°C]			25	70	90	25	70	90	70	90
Mineral	***wt.%***	***vol.%***	**Surface Area [$m^2_{mineral}$ m^{-3}_{bulk}]** **Surface Area [$m^2_{mineral}$ mol^{-1}]**							
brucite	86.9	2.43	$3.8 \pm 0.3 \times 10^5$ $3.2 \pm 0.3 \times 10^2$	1.0×10^4 3.1×10^0	$3.5 \pm 2.5 \times 10^3$ $4.2 \pm 3.0 \times 10^{-1}$	$3.8 \pm 0.3 \times 10^5$ -	$3.5 \pm 2.5 \times 10^3$ $5.4 \pm 4.0 \times 10^{-1}$			
calcite	3.1	0.10	$6.0 \pm 0.1 \times 10^3$ $1.1 \pm 0.9 \times 10^1$			$2.7 \pm 1.2 \times 10^2$ $2.8 \pm 4.0 \times 10^{-1}$				
dolomite	0.6	0.02	$3.0 \pm 2.0 \times 10^{-5}$ $1.1 \pm 0.7 \times 10^{-7}$	$7.0 \pm 2.0 \times 10^{-3}$ $7.2 \pm 2.0 \times 10^{-6}$		$3.0 \pm 2.0 \times 10^{-5}$ $3.4 \pm 2.3 \times 10^{-8}$	$7.0 \pm 2.0 \times 10^{-3}$ $1.1 \pm 0.3 \times 10^{-5}$			
quartz	5.2	0.18	5.5×10^2 $1.8 \pm 0.6 \times 10^{-1}$							
portlandite	3.1	0.12	$6.5 \pm 1.5 \times 10^1$ $5.7 \pm 1.3 \times 10^{-1}$	$4.2 \pm 0.1 \times 10^{-1}$ $6.0 \pm 0.1 \times 10^{-4}$	$3.0 \pm 0.1 \times 10^{-2}$ $3.2 \pm 0.1 \times 10^{-5}$	$6.5 \pm 1.5 \times 10^1$ -	$5.0 \pm 4.0 \times 10^{-1}$ $6.0 \pm 1.3 \times 10^{-4}$			
nesquehonite			$6.1 \pm 0.1 \times 10^6$ $7.0 \pm 0.1 \times 10^2$	*	*	$6.1 \pm 0.1 \times 10^6$ -	*	*	*	*
hydromagnesite	1.1	0.05	$3.0 \pm 2.0 \times 10^{-1}$ $2.0 \pm 1.3 \times 10^{-3}$							
magnesite			*	$2.0 \pm 0.1 \times 10^{-1}$ $2.2 \pm 0.9 \times 10^{-5}$		4.8×10^0** -	$3.0 \pm 2.0 \times 10^0$ $1.2 \pm 0.8 \times 10^{-4}$	$9.9 \pm 0.1 \times 10^1$ $4.8 \pm 0.05 \times 10^{-3}$	$3.0 \pm 2.0 \times 10^0$ $1.9 \pm 1.3 \times 10^{-4}$	$2.9 \pm 0.1 \times 10^2$ $9.9 \pm 0.3 \times 10^{-3}$
aragonite			$5.0 \pm 0.1 \times 10^0$ $2.5 \pm 0.05 \times 10^{-1}$							

vol.% = mineral volume fraction including porosity
*not included in the model
** Sim. B

Table 7

Sample	**Initial**	**1**		**2**		**3**		**4**		**5**		**6**		**7**		**8**	
***p*CO$_2$ [bar]**	atm	10		10		10		50		50		50		74		74	
***T* [°C]**	25	25		70		90		25		70		90		70		90	
time [h]	0	74		72		72		72		72		72		72		72	
		vol.%															
Minerals	Exp.	Exp.	Sim.	Exp.	Sim.	Exp.	Sim.	Exp.	Sim.	Exp.	Sim.	Exp.	Sim.	Exp.	Sim.	Exp.	Sim.
brucite	**83.9**	15.1	3.0	2.3	8.0	17.4	20.7	11.7	0.0	0.0	9.5	7.5	24.3	13.0	35.3	0.0	0.0
calcite	3.5	13.6	9.4	12.1	1.5	5.6	0.0	3.9	38.7	12.8	3.1	3.2	2.5	8.0	3.6	4.4	1.0
dolomite	0.6	0.0	1.8	0.0	6.3	0.0	6.3	0.7	5.7	1.0	4.5	3.0	3.2	4.0	6.0	1.1	6.1
quartz	6.2	3.3	10.4	2.1	5.6	3.8	5.2	4.8	43.4	3.3	6.4	4.3	6.0	4.0	7.0	3.4	5.7
portlandite	4.2	0.0	0.4	0.0	2.3	6.8	3.1	0.0	0.0	5.1	2.7	6.3	3.5	0.0	2.3	0.0	2.6
nesquehonite	0.0	**66.6**	**64.8**	0.0	0.0	0.0	0.0	**77.5**	**0.0**	0.0	0.0	0.0	0.0	0.0	0.0	0.0	0.0
hydromagnesite	1.6	0.0	10.9	**35.1**	**33.3**	**47.5**	**45.7**	0.0	12.1	**5.1**	**1.8**	**12.7**	**1.7**	**19.0**	**2.0**	**0.0**	**1.6**
magnesite	0.0	0.0	0.0	**42.0**	**43.0**	**17.1**	**19.0**	1.4	0.0	**71.7**	**71.9**	**63.1**	**58.8**	**50.0**	**43.9**	**91.2**	**83.0**
aragonite	0.0	1.5	0.1	6.5	0.0	1.7	0.0	0.0	0.1	1.0	0.0	0.0	0.0	2.0	0.0	0.0	0.0

vol.% = mineral content expressed as percentage by volume

Table 8

	Initial Porosity	**Effective diffusion coefficient D_{eff}* [m^2 s^{-1}]**
well boundary conditions	1	4.5×10^{-9}
MgO-based cement (fast)	0.5	1.1×10^{-10}
MgO-based cement (reference)	0.5	1.1×10^{-11}
MgO-based cement (low)	0.5	1.1×10^{-12}
limestone rock	0.1	4.5×10^{-11}

Table 9

Zones	N nodes	grid spacing [m]
well (borehole)	11	0.010
MgO-based cement	13	0.005
	05	0.001
reservoir rock	05	0.001
	10	0.005
	10	0.020
	15	0.050
	20	0.050
	16	0.250
	04	0.250

Table 10

	well (boundary conditions)		MgO-based cement *		reservoir rock	
component	**constraint**	**concentration [mol kgw^{-1}] or pH**	**constraint**	**concentration [mol kgw^{-1}] or pH**	**constraint**	**concentration [mol kgw^{-1}] or pH**
HCO_3^-	pCO_2=150bar, 90°C	1.01×10^0	atm pCO_2 & 90°C	3.8×10^{-4}	charge balance	5.6×10^{-3}
Ca^{+2}	fixed	1.0×10^{-9}	fixed	1.0×10^{-9}	calcite	4.1×10^{-4}
pH	charge balance	3.17	charge balance	5.82	fixed	7.50
Mg^{+2}	fixed	1.0×10^{-9}	fixed	1.0×10^{-9}	dolomite	1.5×10^{-5}
$SiO_{2(aq)}$	fixed	1.0×10^{-9}	fixed	1.0×10^{-9}	fixed	1.0×10^{-9}

* similar composition to CO_2-rich water (boundary conditions) under atmospheric pCO_2 conditions.

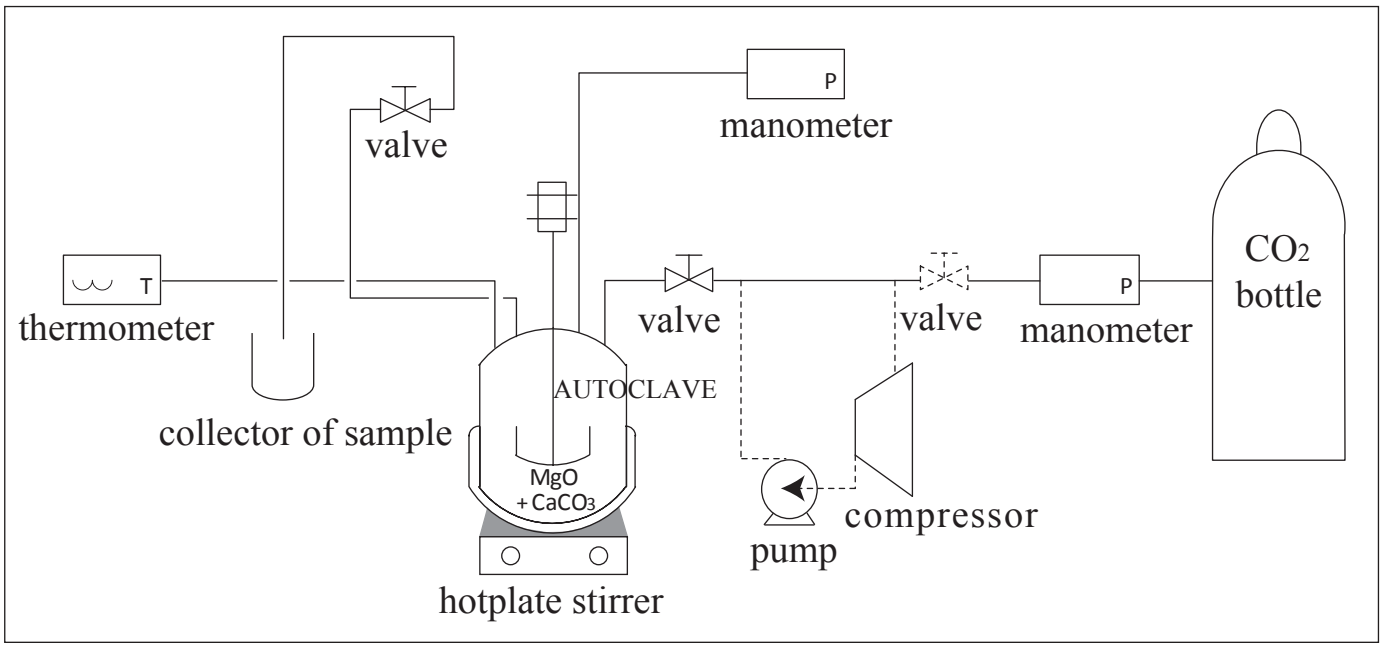
P
manometer
valve
T
thermometer
valve
valve
P
manometer
CO2
bottle
AUTOCLAVE
collector of sample
MgO
+ CaCO3
compressor
pump
hotplate stirrer

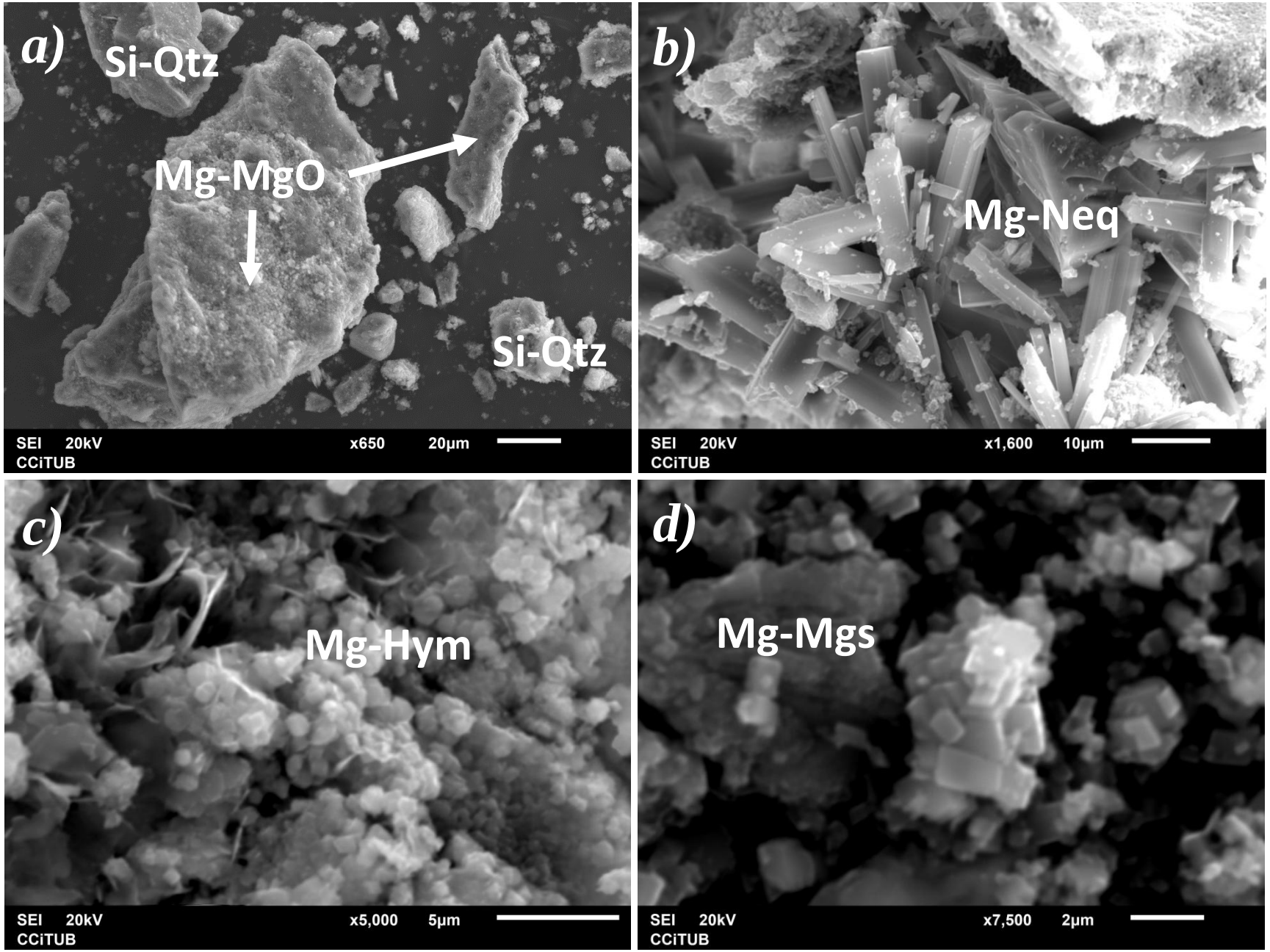
a)
Si-Qtz
Mg-MgO
Si-Qtz
SEI 20kV x650 20µm
CCiTUB
b)
Mg-Neq
SEI 20kV x1,600 10µm
CCiTUB
c)
Mg-Hym
SEI 20kV x5,000 5µm
CCiTUB
d)
Mg-Mgs
SEI 20kV x7,500 2µm
CCiTUB

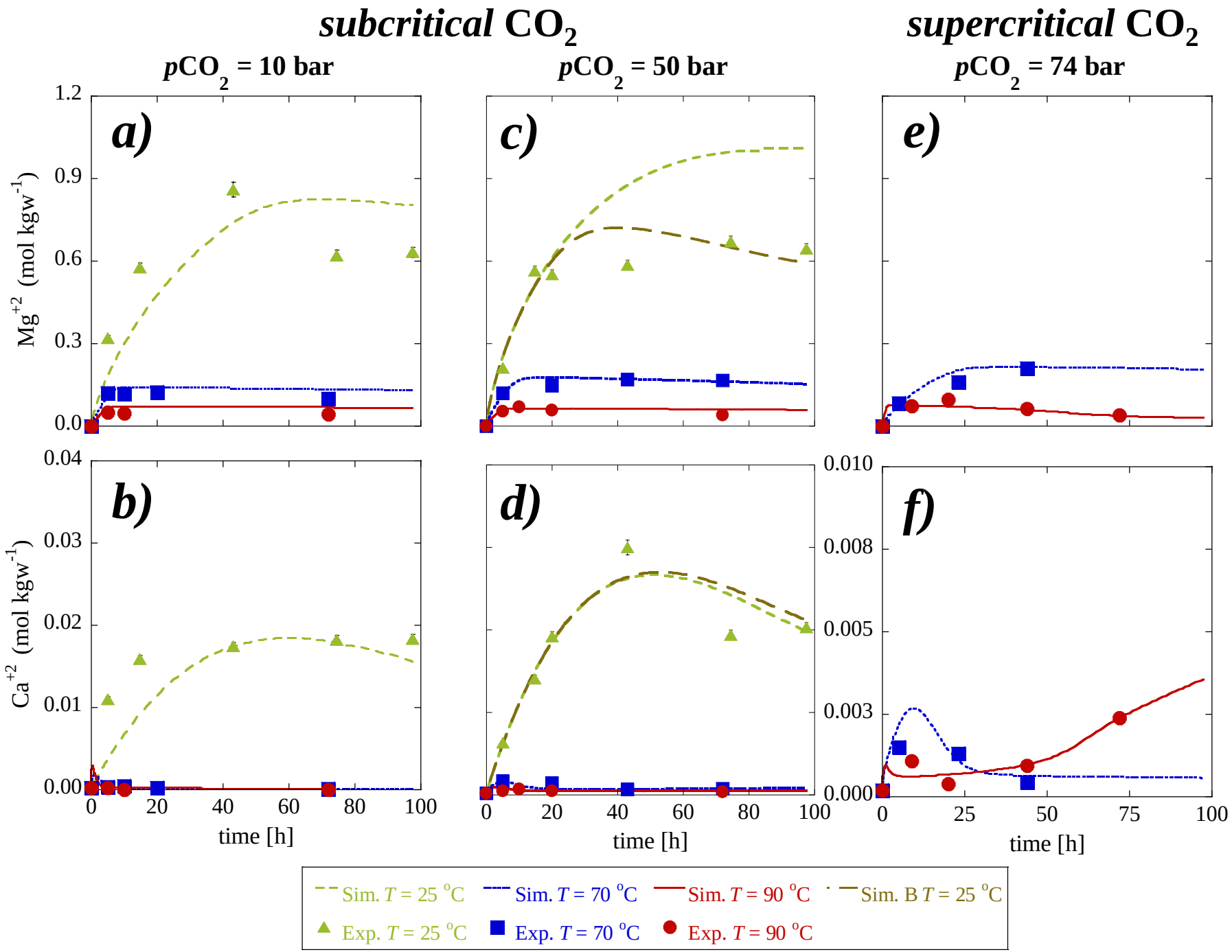
subcritical CO2
supercritical CO2
pCO2 = 10 bar
pCO2 = 50 bar
pCO2 = 74 bar
a)
b)
c)
d)
e)
f)
Mg+2 (mol kgw-1)
Ca+2 (mol kgw-1)
time [h]
Sim. T = 25 °C
Sim. T = 70 °C
Sim. T = 90 °C
Sim. B T = 25 °C
Exp. T = 25 °C
Exp. T = 70 °C
Exp. T = 90 °C

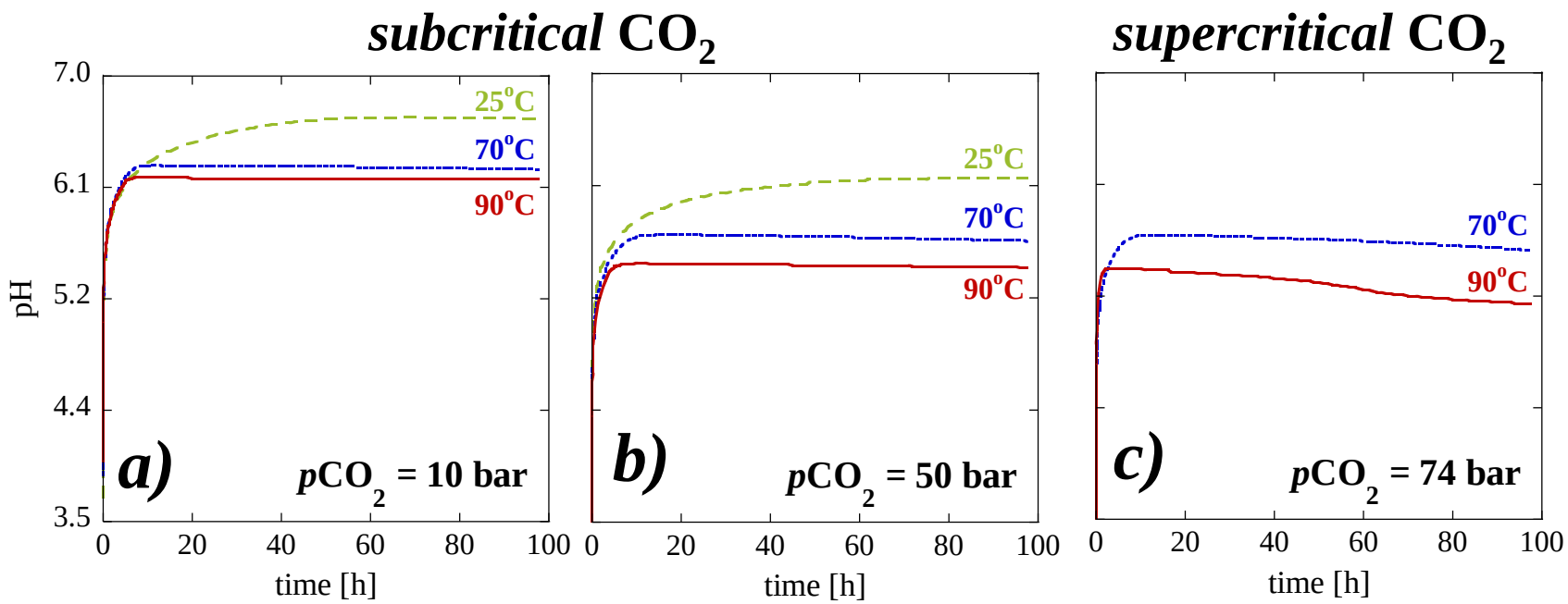
subcritical CO2
supercritical CO2
pH
7.0
6.1
5.2
4.4
3.5
25°C
70°C
90°C
a)
pCO2 = 10 bar
b)
pCO2 = 50 bar
c)
pCO2 = 74 bar
0
20
40
60
80
100
time [h]

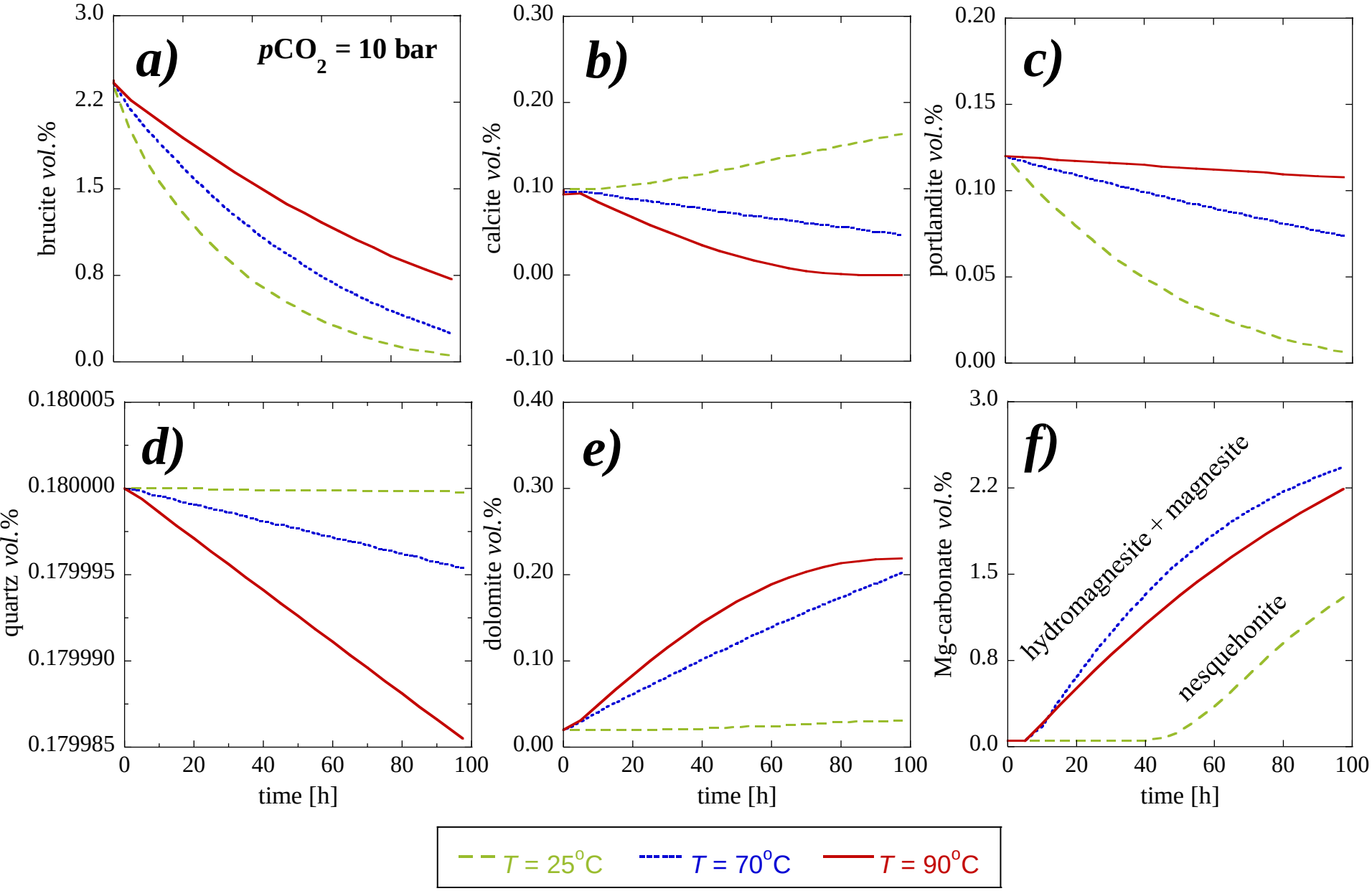
a)
pCO2 = 10 bar
brucite vol.%
b)
calcite vol.%
c)
portlandite vol.%
d)
quartz vol.%
e)
dolomite vol.%
f)
Mg-carbonate vol.%
hydromagnesite + magnesite
nesquehonite
time [h]
T = 25°C
T = 70°C
T = 90°C

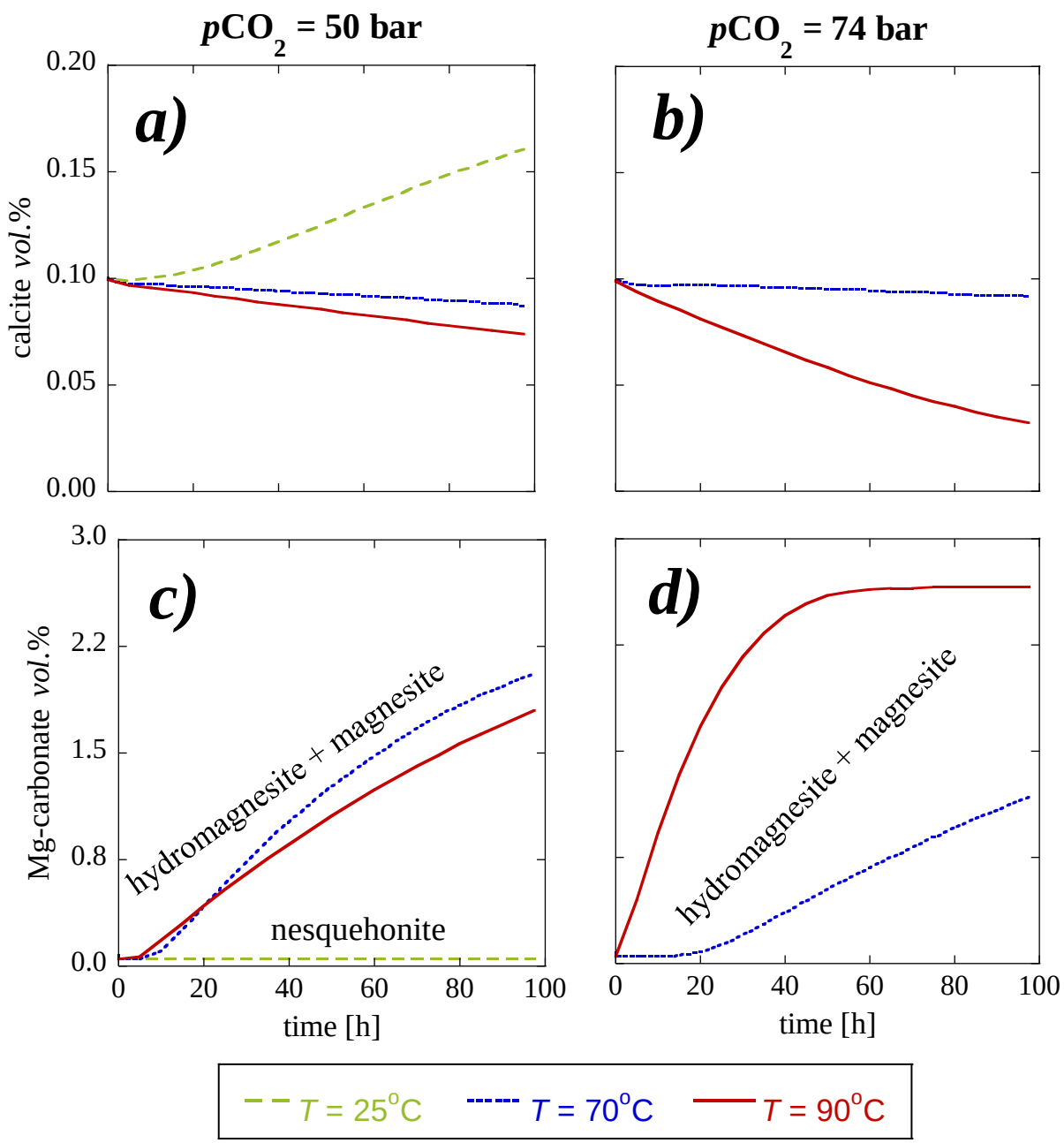
pCO2 = 50 bar
pCO2 = 74 bar
a)
b)
c)
d)
calcite vol.%
Mg-carbonate vol.%
0.20
0.15
0.10
0.05
0.00
3.0
2.2
1.5
0.8
0.0
hydromagnesite + magnesite
nesquehonite
0
20
40
60
80
100
time [h]
T = 25°C
T = 70°C
T = 90°C

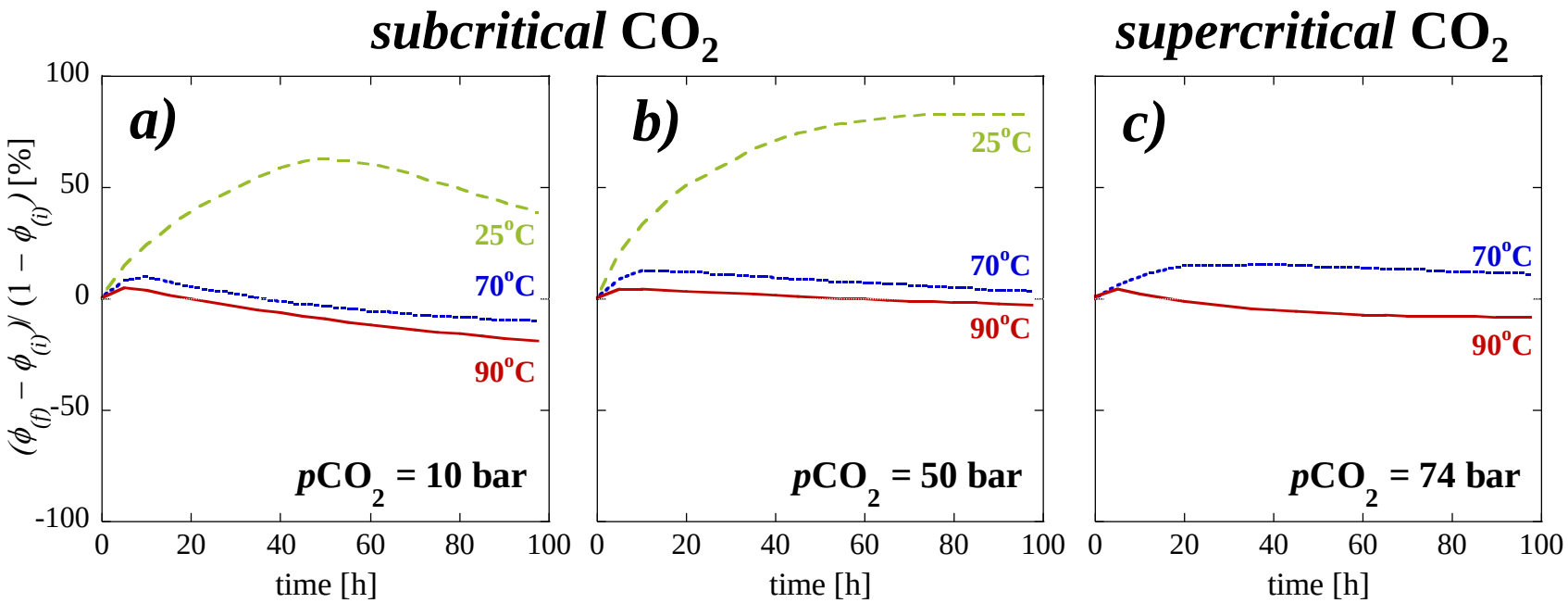
subcritical CO2
supercritical CO2
a)
b)
c)
25°C
70°C
90°C
pCO2 = 10 bar
pCO2 = 50 bar
pCO2 = 74 bar
(φ(f) − φ(i))/ (1 − φ(i)) [%]
100
50
0
-50
-100
0
20
40
60
80
100
time [h]

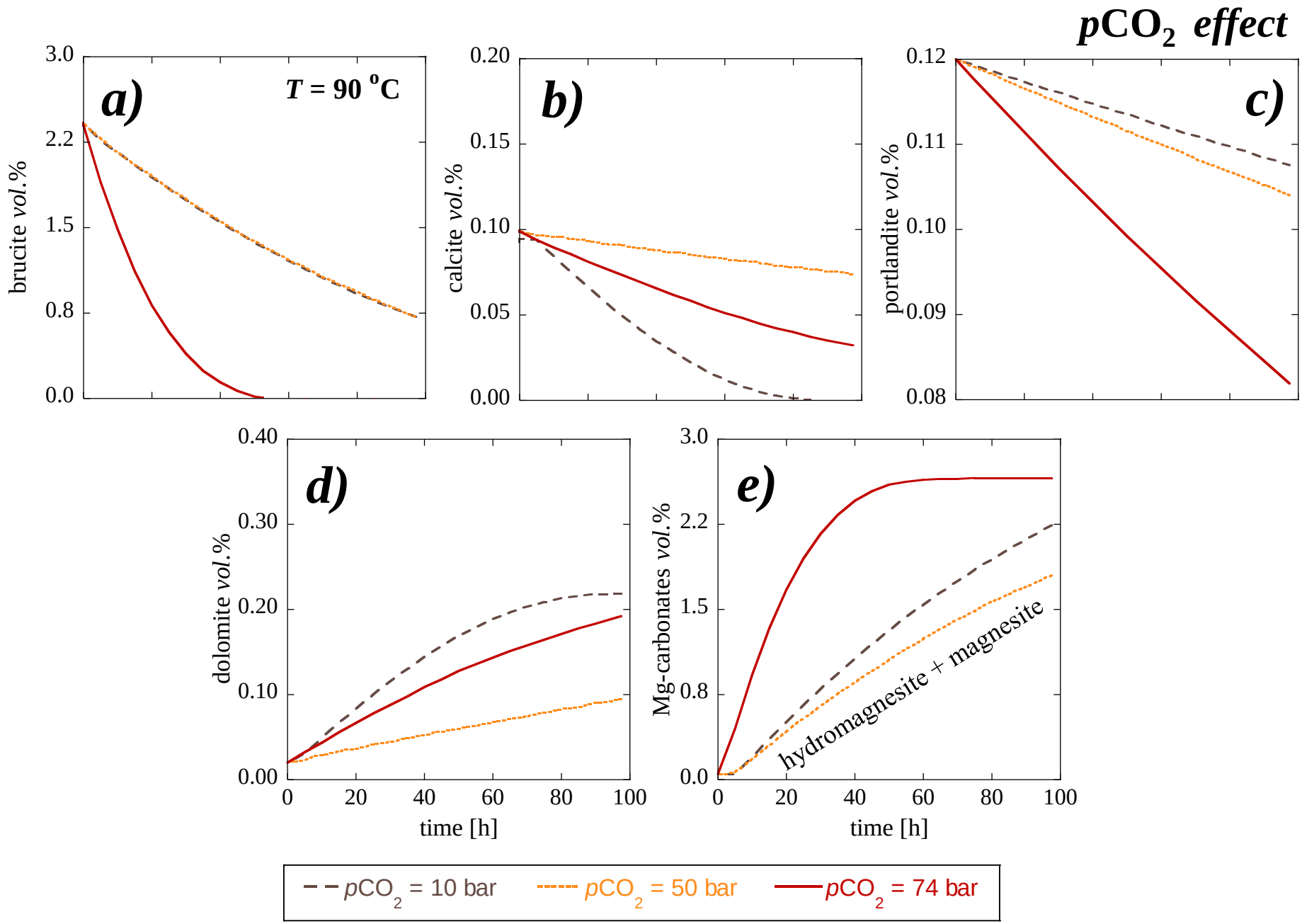
pCO2 effect
a)
T = 90 °C
brucite vol.%
3.0
2.2
1.5
0.8
0.0
b)
calcite vol.%
0.20
0.15
0.10
0.05
0.00
c)
portlandite vol.%
0.12
0.11
0.10
0.09
0.08
d)
dolomite vol.%
0.40
0.30
0.20
0.10
0.00
0
20
40
60
80
100
time [h]
e)
Mg-carbonates vol.%
3.0
2.2
1.5
0.8
0.0
hydromagnesite + magnesite
0
20
40
60
80
100
time [h]
pCO2 = 10 bar
pCO2 = 50 bar
pCO2 = 74 bar

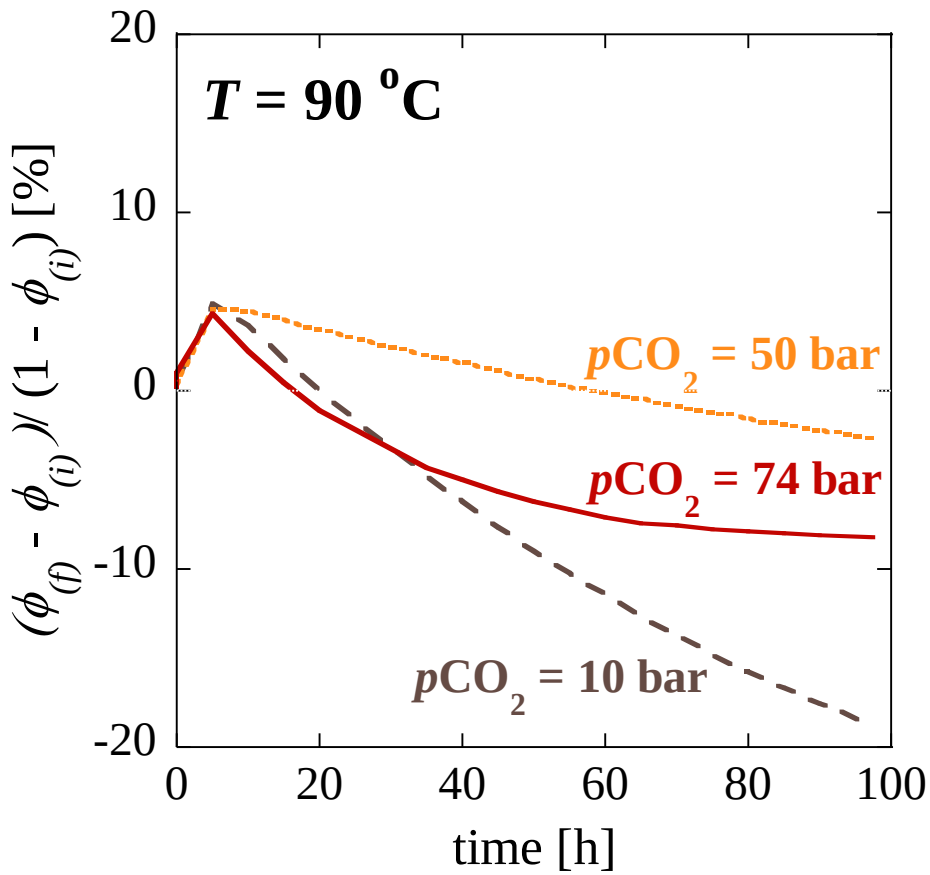
T = 90 °C
pCO2 = 50 bar
pCO2 = 74 bar
pCO2 = 10 bar
(φ(f) - φ(i))/(1 - φ(i)) [%]
time [h]
20
10
0
-10
-20
0
20
40
60
80
100

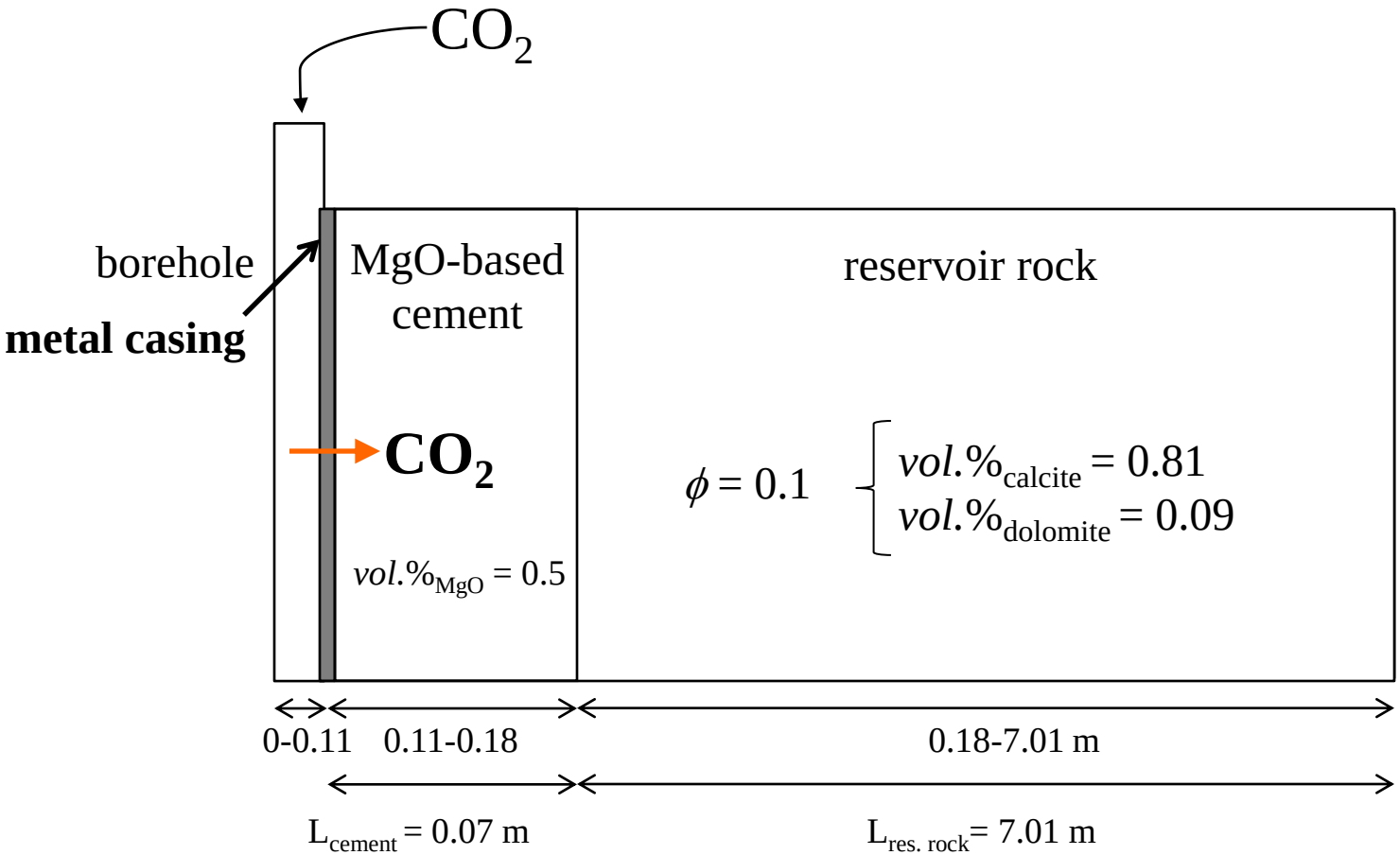
CO_2
borehole
metal casing
MgO-based cement
CO_2
$vol.\%_{MgO} = 0.5$
reservoir rock
$\phi = 0.1$
$vol.\%_{calcite} = 0.81$
$vol.\%_{dolomite} = 0.09$
0-0.11
0.11-0.18
0.18-7.01 m
$L_{cement} = 0.07$ m
$L_{res.\ rock} = 7.01$ m

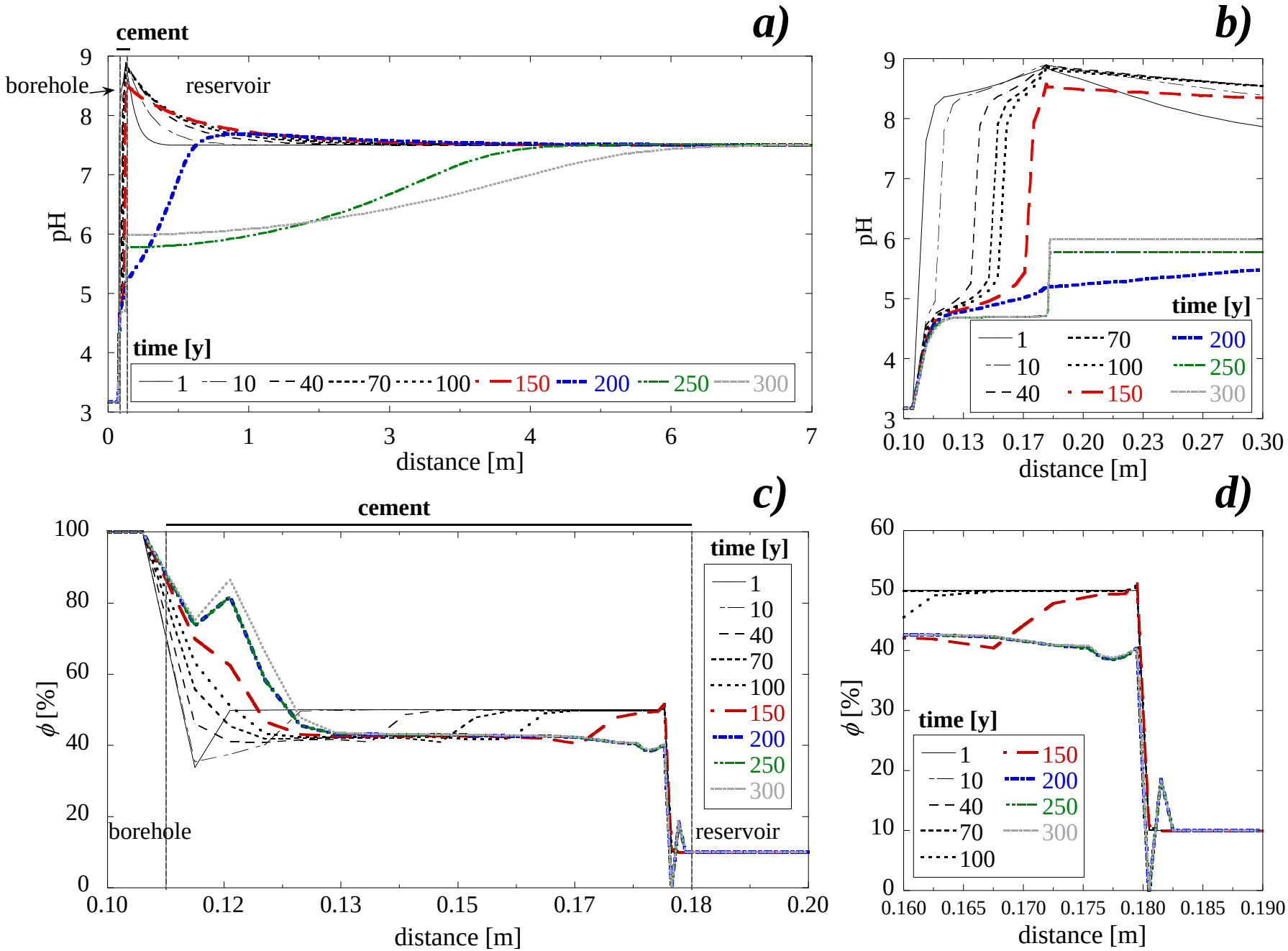
a)
cement
borehole
reservoir
pH
distance [m]
time [y]
1
10
40
70
100
150
200
250
300
b)
pH
distance [m]
time [y]
c)
cement
borehole
reservoir
ϕ [%]
distance [m]
d)
ϕ [%]
distance [m]

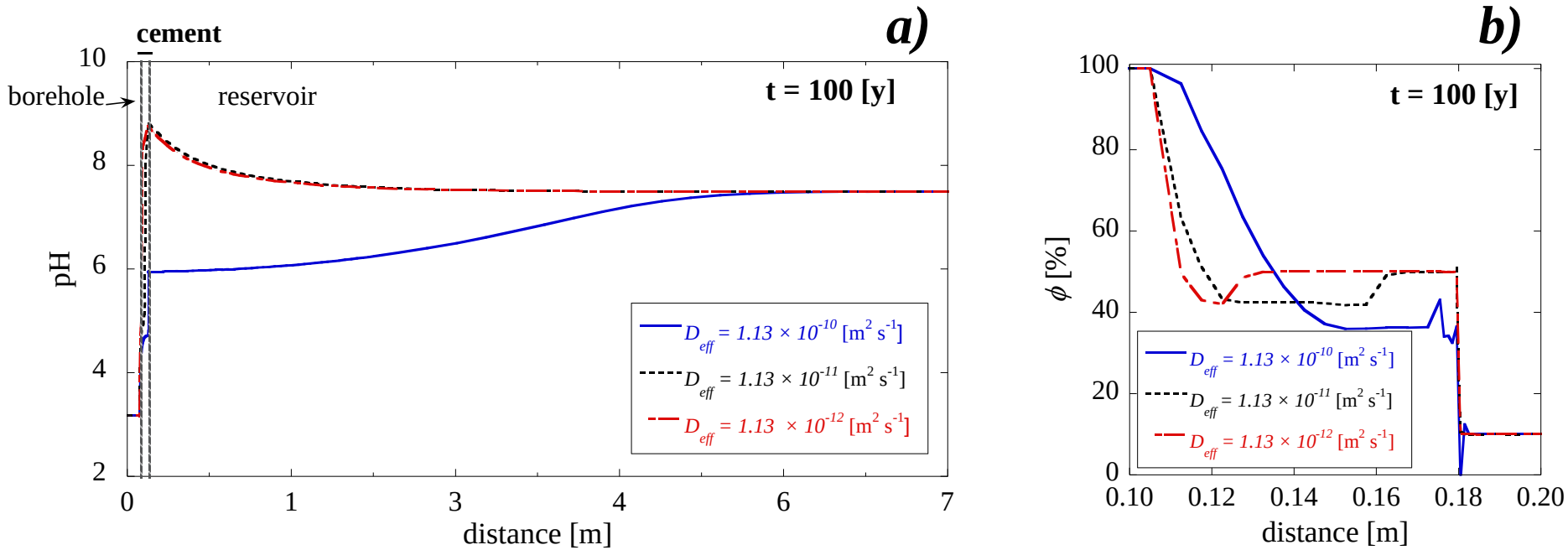
a)
cement
borehole
reservoir
t = 100 [y]
pH
distance [m]
D_{eff} = 1.13 × 10^{-10} [m^2 s^{-1}]
D_{eff} = 1.13 × 10^{-11} [m^2 s^{-1}]
D_{eff} = 1.13 × 10^{-12} [m^2 s^{-1}]
b)
t = 100 [y]
ϕ [%]
distance [m]
D_{eff} = 1.13 × 10^{-10} [m^2 s^{-1}]
D_{eff} = 1.13 × 10^{-11} [m^2 s^{-1}]
D_{eff} = 1.13 × 10^{-12} [m^2 s^{-1}]

Figure S1. Variation of the simulated saturation index (SI_m) of minerals (brucite, calcite, portlandite, quartz, dolomite, nesquehonite, hydromagnesite and magnesite) as a function of time at 25, 70 and 90 C and pCO_2 = 10 bar.

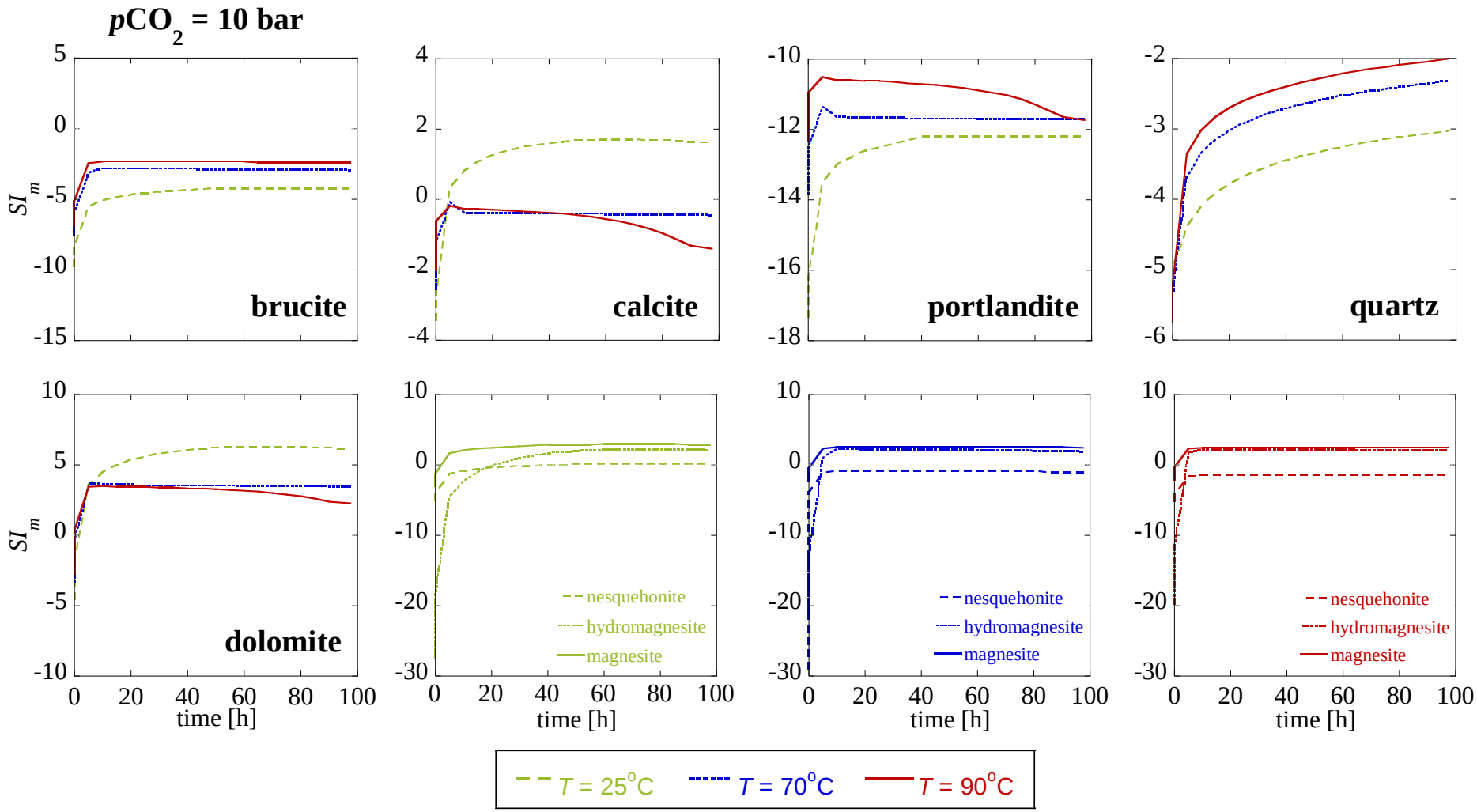

Figure S2. Variation of the simulated mineral dissolution/precipitation rates (R_m) (brucite, calcite, portlandite, quartz, dolomite, nesquehonite, hydromagnesite and magnesite) as a function of time at 25, 70 and 90 C and pCO_2 = 10 bar.

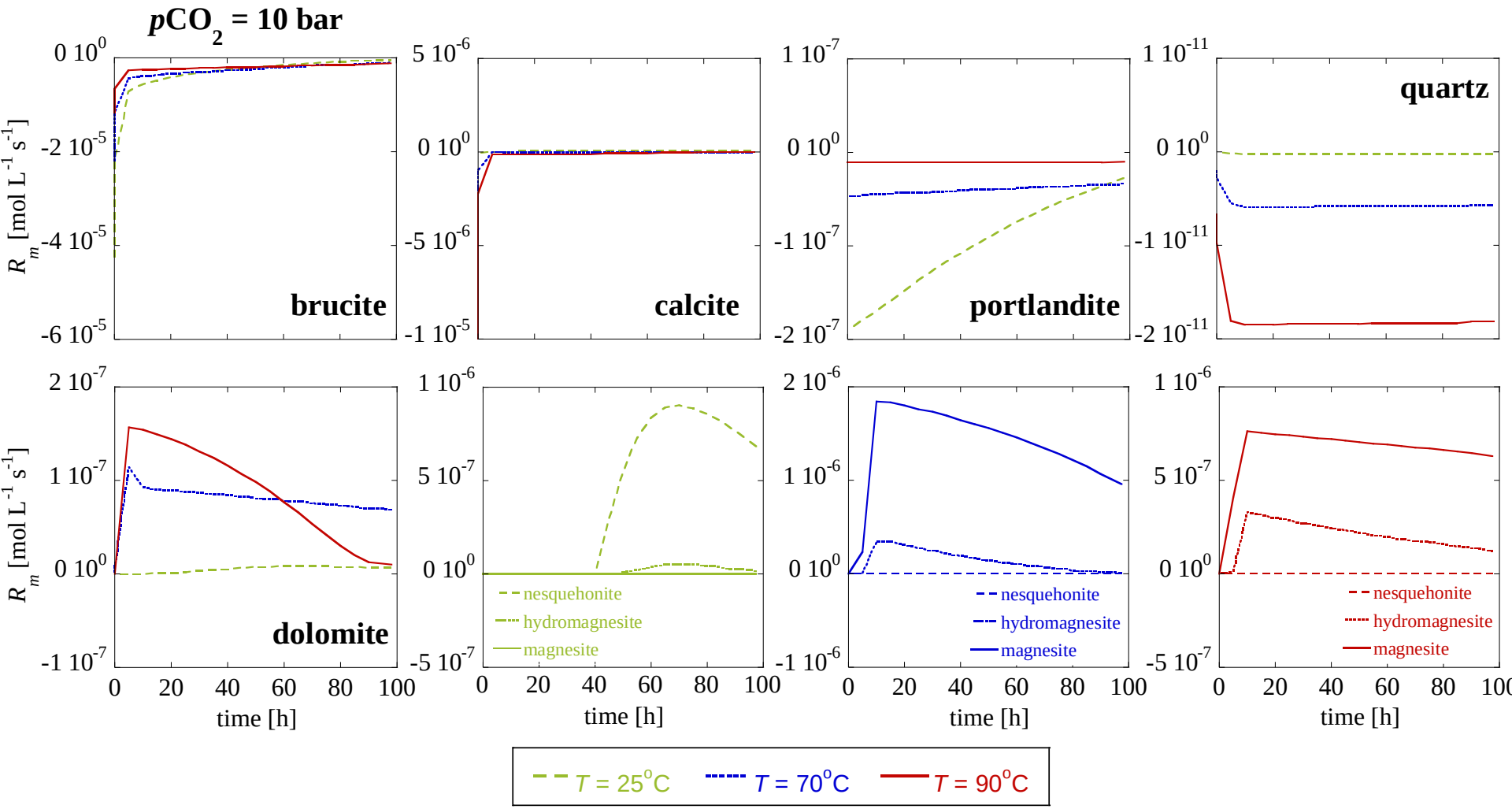

Figure S3. Variation of the simulated saturation index (SI_m) of minerals (brucite, calcite, dolomite, nesquehonite, hydromagnesite and magnesite) as a function of time at 25, 70 and 90 C and pCO_2 = 50 bar.

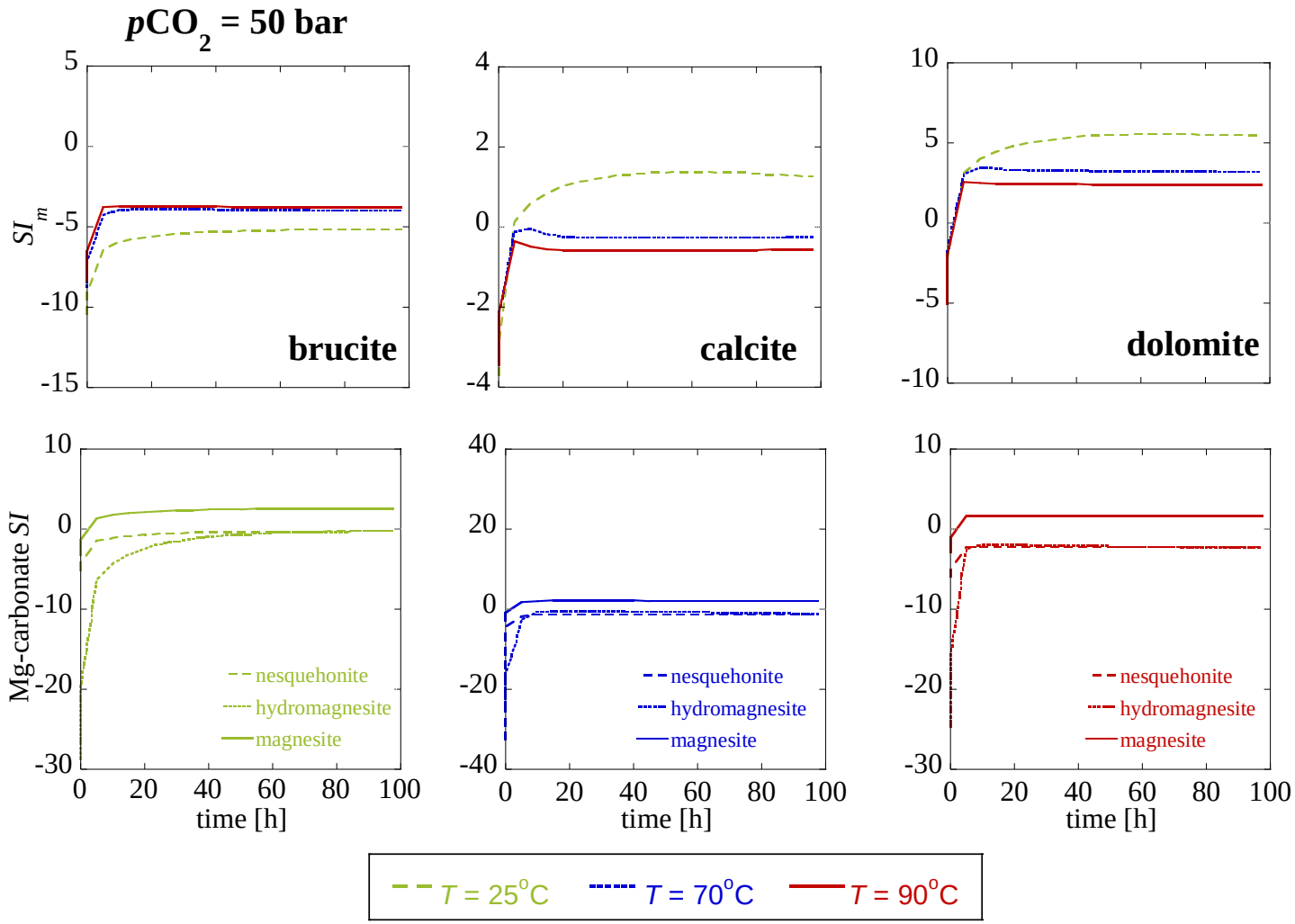

Figure S4. Variation of the simulated saturation index (SI_m) of minerals (brucite, calcite, dolomite, nesquehonite, hydromagnesite and magnesite) as a function of time at 25, 70 and 90 C and pCO_2 = 74 bar.

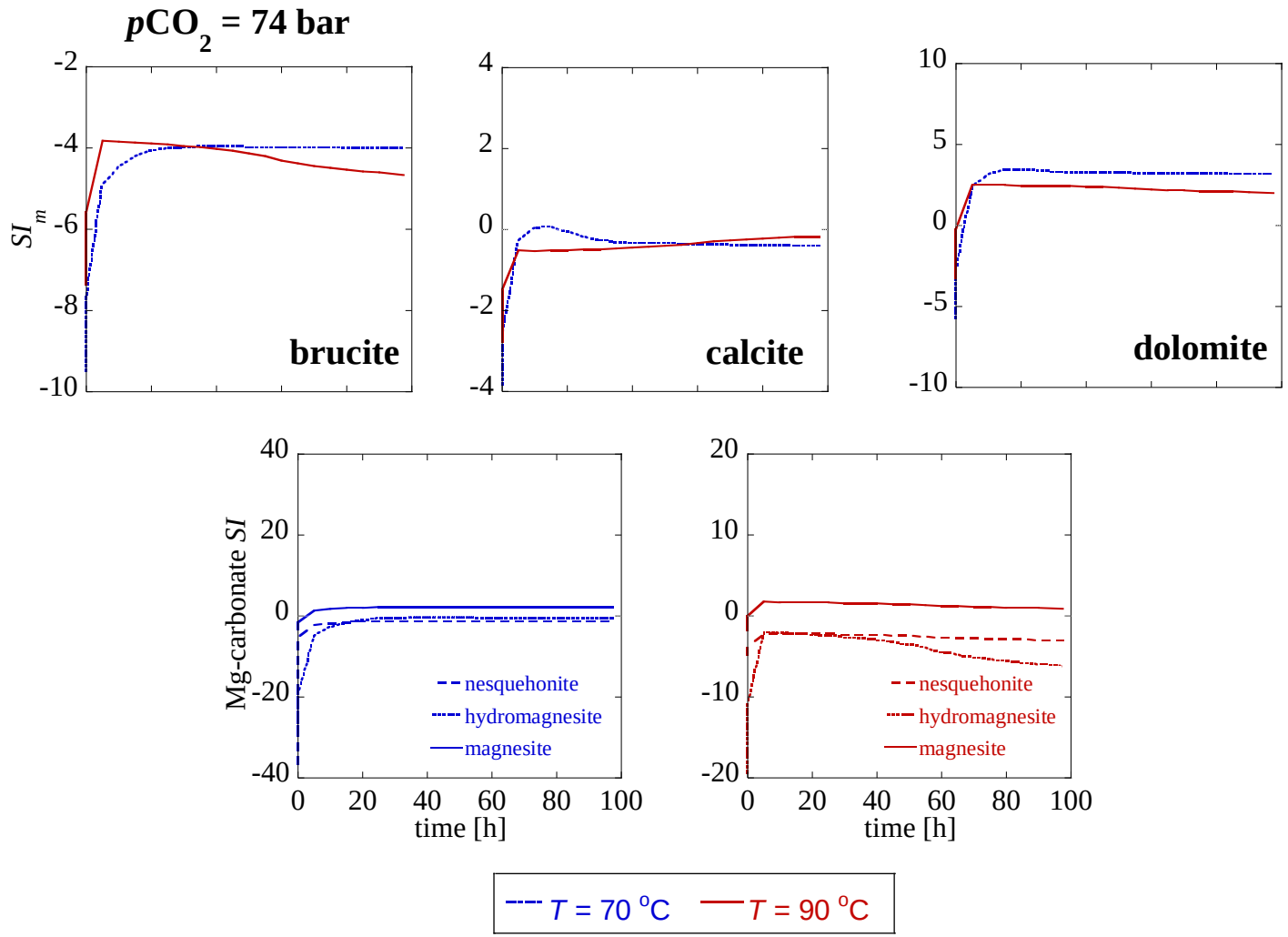

Figure S5. Simulated variation of the mineral dissolution/precipitation rates (R_m) at the borehole-cement interface: borehole from 0 to0.11 m; MgO-based cement from 0.11 to 0.18 m and reservoir rock from 0.18 to 7.01 m.